International Journal of Solid Materials
Vol. 1, Issue 2, 2019, Pages 171-225
Published Online on November 23, 2019

http://jyotiacademicpress.org

COMPUTATIONAL ANALYSIS OF THE MECHANICAL STRENGTH AND DEBONDING PROCESS OF ADHESIVELY BONDED JOINTS

XIANG-FA WU and URACHING CHOWDHURY

Department of Mechanical Engineering
North Dakota State University
Fargo, Narth Dakota 58108
USA
e-mail: xiangfa.wu@ndsu.edu

Abstract

High stress concentration at the free edges of Adhesively Bonded Joints (ABJs) is responsible for their debonding failure. This paper is to investigate the debonding initiation and growth in ABJs by means of a semi-analytic stress-function variational method and Cohesive-Zone-Model (CZM) based Finite Element Method (FEM). In particular, effects of the geometries, material properties, and debonding toughness of the adhesive layers on the free-edge stresses and global load-carrying capacity, i.e., the characteristic full-range load-displacement diagram, of an adhesively single-sided strap joint (ASSSJ) were examined. In the modelling, debonding initiation at the free edges of the ABJs is controlled according to a linear cohesive law in terms of the critical interfacial peeling (Mode-I) and shearing (Mode-II) fracture toughness. Numerical results show that the critical tensile force to trigger the debonding initiation in the ASSSJ increases nearly linearly with increasing interfacial debonding toughness and decreases slightly with increasing adhesive layer thickness. The effective longitudinal stiffness of the ASSSJ is nearly independent of the modulus of the adhesive layer and decreases by increasing

Keywords and phrases: adhesively bonded joints (ABJs), cohesive zone model, fracture mechanics, debonding, finite element method, stress-function variational method.
Communicated by Kazem Reza Kashyzadeh.
Received July 16, 2019; Revised September 18, 2019

adhesive layer thickness. In addition, the full-range load-displacement diagram of the ASSSJ during the entire debonding process exhibits a flat, seemingly, "yield" region corresponding to the stable debonding process, which indicates the excellent, controllable mechanical durability of the ASSSJ. The present studies demonstrate the capabilities of stress-function variational method and CZM-based FEM for determining the load-carrying capacity of ABJs, which are applicable to explore the failure mechanisms, reliable design, active debonding suppression, and extension of the mechanical durability of ABJs for use in broad structures.

1. Introduction

Modern aerospace, aeronautical, and ground vehicles highly depend upon the development and deployment of high-performance materials and structures to fulfill their ever-increasing functionalities including lightweight, high specific strength and stiffness, and excellent agility, durability, and corrosion resistance, among others. Adhesively bonded joints (ABJs) offer a high-efficiency mechanical option for reliable load transfer and connection of separated parts in various structural applications of broad industrial sectors from microscale electronic packaging to macroscale bridge repairing. Figure 1 illustrates a few typical ABJs commonly integrated in a variety of structures. Compared to conventional mechanically fastened bolts as well as riveted and welded joints, ABJs carry several superior advantages such as significantly simplified structural design and fabrication, reduced joining space and weight, enhanced mechanical durability and fatigue tolerance, increased anticorrosion capability, and suppression of noises and material wears [1-4].

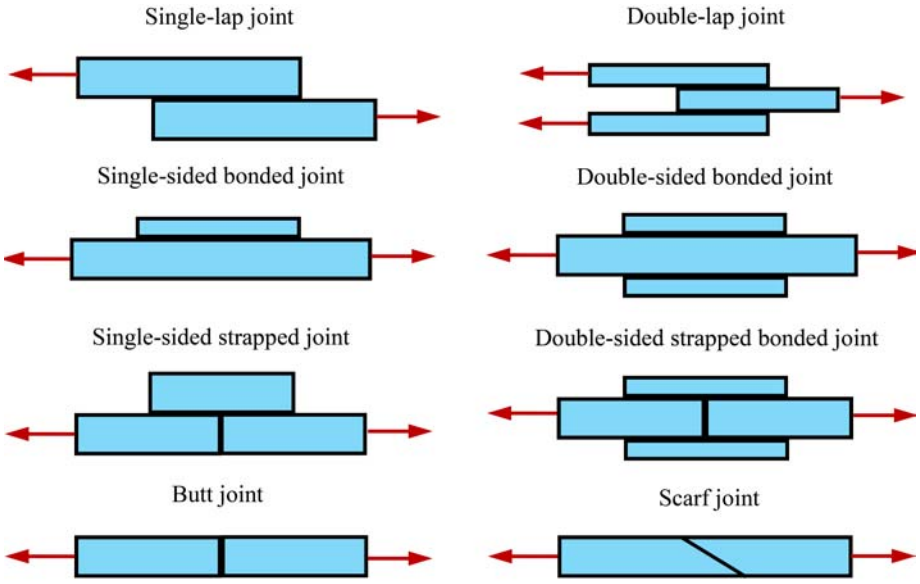

Figure 1. Schematic adhesively bonded joints (ABJs).

Due to the unique geometrical configuration of an ABJ where several identical or dissimilar adherents are joined together by adhesives to form a wedge-like structure at a small region, high stress concentration exists at its free edges as the result of mismatch of elastic properties and coefficients of thermal expansion of the joined materials across the bonding lines [5-8]. Accurate stress analysis of ABJs is deemed fundamental to the structural design and failure analysis of ABJs subjected to external mechanical and thermomechanical loads. Yet, it is rather challenging to accurately solve a set of governing Partial Differential Equations (PDEs) of elasticity to simultaneously satisfy the multiple boundary conditions (BCs) of traction and displacement at the free edges and bonding lines of ABJs. With various extents of simplification and deliberation, several successful ABJ models have been developed for determining the stress field of ABJs. Historically, Volkersen [9], Goland and Reissner [10] are the pioneers in stress analysis of ABJs, who first formulated the systematic approaches to

calculate the approximate stress fields in ABJs within the framework of elasticity. Their treatments of the adhesive layers of ABJs have been extensively adopted by many later investigators in this area, in which Volkersen [9] has regarded the adhesive layer as a simple one-dimensional (1D) shear spring, while Goland and Reissner [10] have simplified the adhesive layer as a uniformly stressed layer with no stress variation across the layer thickness. As a matter of fact, Volkersen's and many follow-ups' stress field solutions of ABJs do not satisfy the simply shear-free condition at the free edges. Goland and Reissner's solutions are able to satisfy the traction conditions at the free edges while the traction-free conditions at the top and bottom surfaces of the adherents are not exactly satisfied though various elasticity approaches in their work were used to suppress such fictitious surface stresses.

By adopting the fundamental assumptions of ABJs by Volkersen [9], Goland and Reissner [10], a number of ABJ models have been established to improve the accuracy of stress analysis of bonded joints and ABJs in the past three decades. Delale et al. [11] have formulated a general ABJ model capable of universally determining the stress field in adhesively bonded single-lap joints and single-sided strap joints, in which the adherent layers are treated as elastic plates under cylindrical bending and the deformations across the adhesive layer are assumed to be constant. However, the shear stress predicted by this model does not satisfy the shear-free condition at the adherent ends. In addition, refined Finite Element Analysis (FEA) indicated that the interfacial stresses predicted by this model are overshot in a large region from the adherent ends [12]. Chen and Cheng [13] have proposed an ABJ model for stress analysis of adhesively bonded single-lap joints by assuming that the axial stresses are linearly varying across the adherent thickness (i.e., *Euler-Bernoulli beam*) and the shear stress is constant across the adhesive layer. In this model, the entire stress field in the ABJ can be expressed in terms of two unknown normal stress functions via triggering the stress equilibrium equations in two-dimensional (2D) elasticity. These two unknown stress functions can be further determined via solving two

coupled 4th-order Ordinary Differential Equations (ODEs) according to the principle of complementary strain energy. The stress field gained in this ABJ model can satisfy all the traction BCs, and the predicted location of the peak interfacial shear stress appears at a distance of ~20% the adherent thickness from the adherent ends as validated quantitatively by FEA [12, 14-16]. However, due to the over simplification of the adhesive layer, this ABJ model yields a physically questionable zero normal stress in the adhesive layer along the bonding line. In addition, by using a simple shear-lag model of the adhesive layer and ignoring the bending effect of the adherents. Her [17] has obtained the closed-form solutions to the axial force in adherents and the shear-force in adhesive layer of adhesively bonded single/double-lap joints, respectively. But, the static equilibrium of the joint and the shear-free conditions at the adherent ends are not satisfied. Tsai et al. [18] have extended the classic ABJ model formulations by Volkersen [9], Goland and Reissner [10] via adopting a linear variation of the shear deformation across the adhesive layer. This model is able to recover the classic Volkersen's, Goland and Reissner's models in the limiting cases. Furthermore, by modelling the adhesive layer as two distributed linearly elastic shear and tension springs, Lee and Kim [15] have derived the closed-form solutions to the axial force in adherents and the shear force in adhesive layer of adhesively bonded single-lap joints, which were validated by their detailed FEA except that the shear-free conditions at the adherent ends are not satisfied. Radice and Vinson [19] have formulated a higher-order ABJ model, in which the Airy stress potential for 2D elastic ABJ body is expressed as a series of power functions with respect to the thickness coordinate and is consequently determined via solving the resulting *Cauchy-Euler* equations in favor of *Rayleigh-Ritz* minimization of the potential energy of the ABJs. Recently, Khan et al. [20] have formulated a theoretical ABJ model to take into account the effect of transverse shear of the ABJ adherents. In their model, the ABJ adherents are treated as Timoshenko's beams and this model was used to guide reduction of the interfacial shear and peeling stresses via material tailoring.

In addition, several layer wise joint models have been formulated for improving the stress analysis of ABJs. For instance, Hadj-Ahmed et al. [21] have formulated a layer wise ABJ model with the multi-layers of the ABJ to be modeled as a stack of Reissner plates that are coupled through the inter laminar normal and shear stresses. The governing equations of the ABJs are obtained via minimizing the strain energy of the ABJ. Diaz et al. [16] have proposed an improved layer wise ABJ model, in which the ABJ was modeled as a stack of Reissner–Mindlin plates. As a result, a set of eight governing ODEs was extracted via evoking the constitutive laws and solved to satisfy the traction BCs. This ABJ model can be well validated by FEA for free-edge interfacial stress prediction. Moreover, Yousefsani and Tahani [22, 23] have provided another version of the layer wise ABJ model. In their model, the displacements of artificially divided sub-layers of an ABJ were treated as field variables, and a set of governing ODEs was obtained via minimizing the potential energy of the joint. For accurate interfacial stress prediction, 18 artificial sub-layers were used in their numerical examples. Such layer wise ABJ models were further extended for stress analysis of smart joints integrated with piezoelectric patches in their recent efforts [24].

Furthermore, to approach well-conditioned interfacial stresses in ABJs, especially to satisfy the traction-free conditions at the multiple free-edges of ABJ adherents, earlier investigations by Chang [25-28] introduced sine and cosine series expansions of the interfacial peeling and shear stresses on the bonding lines with their coefficients to be determined via minimizing the strain energy of the ABJs, in which the axial stresses in the elastic adherents are assumed to be linearly varying across the adhered thickness as that of classic *Euler-Bernoulli beam* theory. In principle, Chang's approach is exact, without adoption of additional simplifications beyond the classic *Euler-Bernoulli beam* theory; the interfacial stress solutions are expressed as the sums of infinite trigonometrical series, which can be further calculated in elegant closed-form expressions. But, refined FEA indicates that Chang's

approaches carry noticeable stress deviations near the free edges of ABJs, due mainly to the harsh treatment of the deformation (deflection) compatibility of (adhesively) bonded dissimilar adherents in bending within the framework of *Euler-Bernoulli beam* theory of composite beams [29, 30].

To overcome the above theoretical obstacle in stress analysis of ABJs within the classic *Euler-Bernoulli beam* theory, Wu et al. [2, 3, 12, 30-32] have formulated a general high-efficiency stress-function variational method for accurate determination of the interfacial stresses in a variety of ABJs including bonded joints and adhesively bonded monolithic and composite joints. In the process of this method, two unknown interfacial shear and normal (peeling) stress functions are adopted at each interface; the axial stresses in the adherents and adhesive layers are both assumed to be linearly varying across the thickness as that of classic *Euler-Bernoulli beams*. By evoking the 2D stress equilibrium equations, the rest planar stress components in the ABJs are expressed exactly in terms of the unknown interfacial stress functions [33]. Such treatment is able to guarantee that all the stress components are consistent across the bonding lines [3]. Finally, these unknown interfacial stress functions are determined via solving a set of coupled ODEs, which is extracted according to the complimentary strain energy of the joints, to satisfy the deformation compatibility across the interfaces in the weak form without adoption of additional assumptions. In the simple case of bonded joints made of two adherents, a set of two coupled ODEs with respect to two interfacial stress functions can be obtained [2, 31]; in the case of ABJs made of two adherents adhesively bonded through an adhesive layer, a set of four coupled ODEs with respect to two pairs of the interfacial shear and peeling stress functions at two interfaces are obtained [3, 12]. The interfacial shear and peeling stresses of the ABJs determined by this method can exactly satisfy the traction-free conditions at the free edges of the adherents; by using finite element method (FEM), numerical validation indicates the high accuracy of this semi-analytic stress-

function variational method for stress analysis of ABJs [2, 3]. Moreover, this method can be conveniently extended for stress analysis of adhesively bonded composite joints with the adherents made of angle-plied composite laminates [34-37]. More detailed review of recent development of stress analysis of ABJs can be found in review papers [38-42] and relevant references therein.

Though the above analytic and semi-analytic methods as well as various FEMs are capable of determining the interfacial stresses of ABJs in high accuracy, these methods are unsuitable for predicting the debonding process of ABJs, especially the characteristic load-displacement diagram during the entire debonding process. So far, fracture mechanics models have been developed for determining the stress intensity factor and fracture toughness based on various fracture tests of layered structures and ABJs [43-51]. However, these fracture models are unable to analyze and predict the general debonding process in ABJs. On the other side, in modelling the fracture mechanisms in solids, CZM has been typically adopted at the front of a crack tip [52-54], which eliminates the stress singularity at crack tip and therefore makes the fracture event physically more meaningful as well as the computational simulation of crack growth more tractable. Several CZMs have been formulated and successfully integrated into FEMs [55] and available in commercial FEM software packages such as ANSYS®. CZMs are typically classified according to their effective traction-separation relationships such as cubic polynomial, trapezoidal, smoothed trapezoidal, exponential, linear softening, and bilinear softening CZMs, among others. So far, CZM-based FEMs are broadly utilized for modelling crack initiation and propagation in monolithic and composite materials as well as debonding growth in ABJs. Among a large number of CZM-based studies of fracture and debonding initiation and growth in various materials and ABJs, Feraren and Jensen [56] have performed CZM-based FEA of interface fracture near flaws in ABJs to understand the effects of location and direction of the crack growth on the joint

strength. Gustafson and Was [57] have investigated the influence of adhesive constitutive parameters in CZM-based FEA of ABJs including Double Cantilever Beam (DCB), End-Notched Flexure (ENF), and Single Lap Joint (SLJ) models, and pointed out that the model results of DCB model mainly depend upon one parameter of the CZM, while ENF and SLJ models depend upon multiple parameters of the CZM. In their CZM-based FEA, a parameterized trapezoidal traction law was used, which was controlled by the cohesive strength, critical energy release rate, and the trapezoidal shape factor for both Mode-I and Model-II cases. Furthermore, de Moura and Goncalves [58] have utilized CZM-based FEM to simulate the high-cycle fatigue crack growth in ABJs under Mode-I loading, in which Mode-I DCB specimen was considered and a bilinear CZM was adopted. Their numerical results were in excellent agreement with several Paris laws employed as input and showed a great potential of the CZM-based FEM for predictive fatigue analysis of ABJs. In addition, Carneiro and Campilho [59] have conducted the CZM-based FEA of adhesively bonded *T*-joints to evaluate the influence of adhesive fillings on the stress distribution, damage evolution, and the strength of the joints. These studies have demonstrated the great potential of CZM-based FEMs for computational prediction of the initiation and growth of cracks and debonding. Detailed progress on CZM and related numerical implementation for crack growth simulation can be found in the recent review paper by Park and Paulino [55].

With above detailed review on ABJs and related analytical and numerical methods for stress analysis and debonding prediction, the present study is planned in two categories. First, the robust stress-function variational method developed by the first author and his co-workers [2, 3] is further utilized to examine the effects of elastic modulus and thickness of the adhesive layer on the interfacial shear and peeling stresses of an adhesively single-sided strap joint (ASSSJ) in Subsection 2.1. The gained interfacial stresses are to be used as a *prior* to predict the debonding initiation, which is validated by CZM-based FEM

in Subsection 2.2. Second, CZM-based FEM is adopted to simulate the entire debonding process of the ASSSJ and to extract the characteristic full-range load-displacement diagram of the ABJ. Dependencies of the full-range load-displacement diagram upon the geometries, material properties, and debonding toughness of the adhesive layer are examined in details. Discussions of the computational results on the design, durability extension, and failure analysis of ABJs are made. Finally, concluding remarks are drawn in consequence.

2. Problem Formulation and Solution

Debonding failure in ABJs initiates at the interfaces between adherents and adhesive layers near the free edges due to localized stress concentrations and then grows continuously along the bonding lines till the complete debonding of the adhesive layers. Without loss of generality, the computational study herein is to determine the interfacial stresses and the entire debonding process of an ASSSJ made up with a slender cover layer adhesively bonded onto two identical slender substrate layers as illustrated in Figure 2(a). Geometries of the model joint are assumed as the follows. The uniform cover layer carries the length $2L$, thickness h_1, and width b; the uniform substrate layers have the thickness h_2, width b and length much larger than L; the thickness of the uniform adhesive layer is h_0. The coordinate systems are selected such that the x-coordinate is made from the symmetric mid-span of the joint to direct along the layer axis; y_1, y_2, and y_0, respectively, are the coordinates with the origins located at the centroids of cross-section of the cover, substrate, and adhesive layer. The substrate layers are under uniaxial tension of a pair of collinear tensile forces P_0 far away the cover layer.

In reality, ABJs with a finite width are typically in a general three-dimensional (3D) stress state, especially near the free edges and corners of the ABJ adherents. To simplify the process, the ASSSJ under the present consideration is treated in the two-dimensional (2D) *plane-stress*

state and no residual stresses exist in the initial load-free state at the reference temperature. Temperature change ΔT is treated as uniform throughout the joint. The adherents and adhesive layer are treated as isotropic, linearly thermo-elastic solids. For the convenience of the model formulation, parameters and variables with subscripts 1, 2, and 0 stand in the cover, substrate and adhesive layers, respectively. In addition, the stress field gained in the *plane-stress* state can be conveniently converted to that in the 2D *plane-strain* state by simply replacing the Young's modulus (E_i) by $(1-\upsilon_i^2)/E_i$, Poisson's ratio υ_i by $\upsilon_i/(1-\upsilon_i)$, and coefficients of thermal expansion α_i by $(1+\upsilon_i)\alpha_i$, where i = 0, 1, and 2.

2.1. Interfacial stress analysis of ABJs by stress-function variational method

The primary stress-function variational method for stress analysis of bonded joints and ABJs has been formulated in the recent studies by the first author and his co-workers [2, 3]. The derivations of this method were summarized in the Appendix, where the interfacial shear and peeling stresses of an ASSSJ were determined in high accuracy and validated by detailed FEA. The stress-function variational method is further utilized herein to examine the effects of the adhesive modulus and thickness on the interfacial stress variations and to further correlate to the debonding failure predicted by CZM-based FEA in the present study.

For the present ASSSJ, the stress analysis was made on the right symmetric half-portion (Figure 2(b)); the nontrivial shear and peeling stresses on the bonding interfaces are illustrated in Figure 2(c). The high interfacial stresses at the free edges are responsible for the debonding failure of the joint. In addition, CZM-based FEA is further adopted for predicting the entire debonding process and the load-carrying capability of the joint in Subsection 2.2.

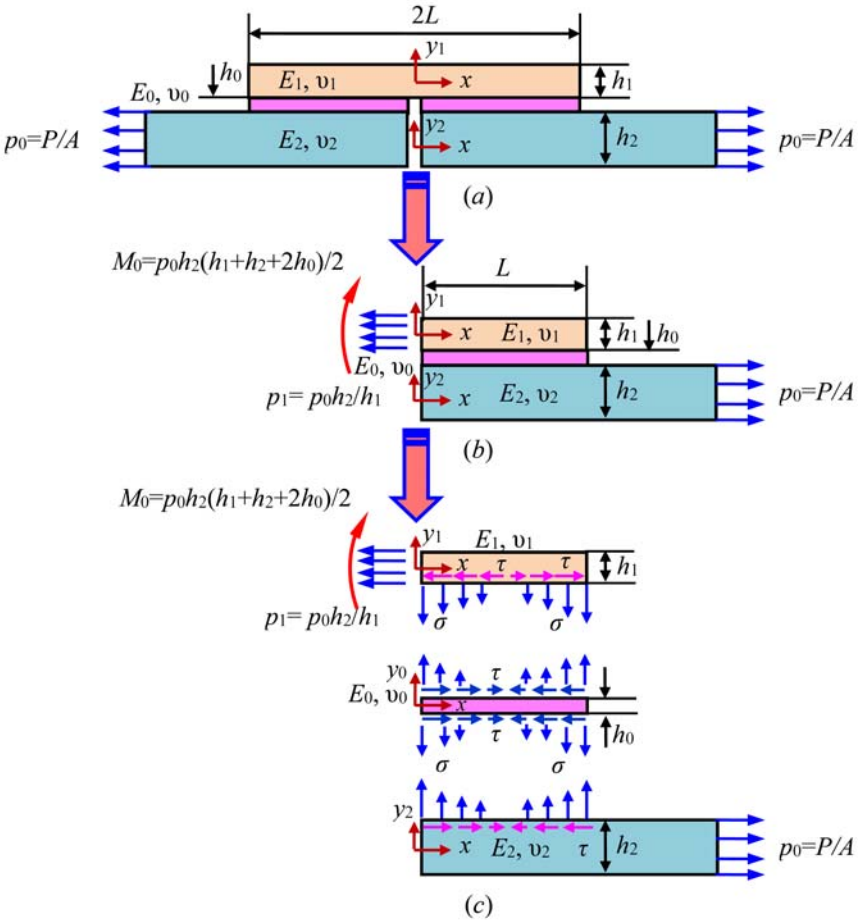

Figure 2. Schematic of an adhesively single-sided strap joint (ASSSJ) and related shear and peeling stresses: (a) the joint is made up with a slender cover layer adhesively bonded onto two identical slender substrate layers, (b) the right symmetric half-joint, and (c) schematic shear and peeling stresses on the adhesive layer.

Due to loss of lateral structural symmetry, the ASSSJ undergoes planar elongation and lateral deflection. The adherents and adhesive layers of the ASSSJ were treated to be slender, and their axial stresses were assumed to be linearly varying, following the classic *Euler-Bernoulli beam* theory, while the shear and lateral normal stresses were

determined by triggering the 2D stress equilibrium equations. Free-body diagrams (FBDs) of the representative segments of the cover, substrate and adhesive layers are shown in Figures 3(a)-(c), respectively, in which the stresses and related stress resultants, i.e., the axial force S_i, shear force Q_i, and bending moment $M_i (i = 0, 1, 2)$, are defined to follow the standard sign conventions in *Mechanics of Materials* [29].

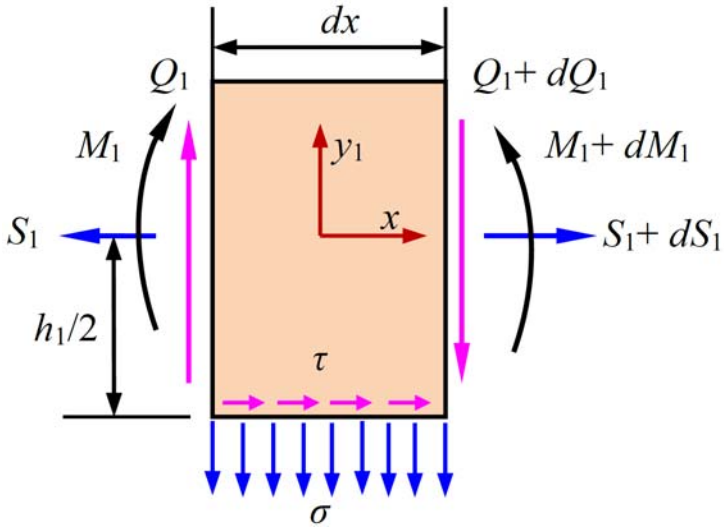

(a)

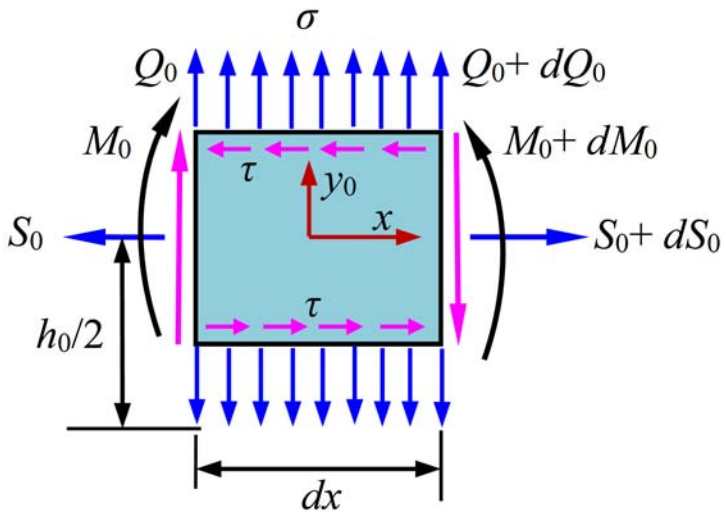

(b)

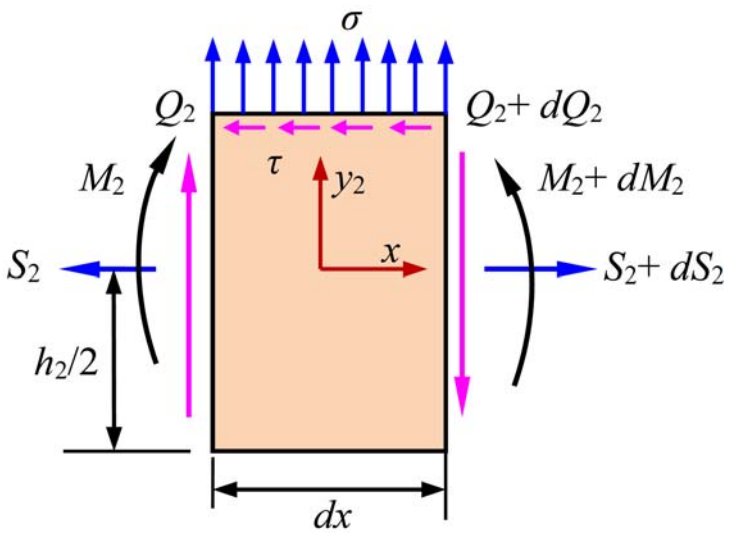

(c)

Figure 3. Free-body diagrams of the representative differential segmental elements of the adhesively single-sided strap joint (ASSSJ): (a) the cover layer, (b) the adhesive layer, and (c) the right substrate layer.

The unique feature of the stress-function variational method is for defining a pair of independent shear and normal (peeling) stress functions at each interface of the joint. For the present ASSSJ, the unknown interfacial shear and peeling stress functions on the upper and lower interfaces are defined as [3]:

$$\tau_1 = f_1(x),\ \sigma_1 = g_1(x),\ \tau_2 = f_2(x), \text{ and } \sigma_2 = g_2(x). \tag{1}$$

The shear-free conditions at the adhered edges at $x = 0$ and L specify:

$$f_1(0) = f_1(L) = 0, \text{ and } f_2(0) = f_2(L) = 0. \tag{2}$$

The rest traction conditions of the axial tractions, shear-forces and bending moments at the upper/lower adhered and adhesive layer ends of the ASSSJ as well as the process for solving the stress functions $f_1(x)$, $f_2(x)$, $g_1(x)$, and $g_2(x)$ are listed in Appendix.

To examine the dependencies of the interfacial shear and peeling stresses upon the adhesive modulus and thickness, as shown in Figure 2, the ASSSJ is considered to be made of a steel (St) cover layer (E_1 = 210 GPa, υ_1 = 0.30) and two identical aluminum (Al)-alloy substrate layers (E_2 = 70GPa, υ_2 = 0.33), which are adhesively bonded together through an epoxy-type adhesive with varying elastic modulus (E_0 = 5, 10, and 20GPa, and υ_1 = 0.48) and thickness (h_0 = 0.2, 0.5, 0.7, and 1.0mm). The adherents and adhesive layers have the same width; other geometries of the joint are: h_1 = 2.0mm (steel), h_2 = 2.0mm (Al-alloy), and L = 20mm (see Figure 2). A uniform tensile traction of the magnitude p_0 = 1.0MPa was applied to the substrate layers. By using the stress-function variational method, Figures 4-6 show detailed numerical results of variations of the interfacial shear and peeling stresses at the upper and lower interfaces of the ASSSJ. In each figure, the shear and peeling stress variations are plotted on the upper and lower interfaces separately at four different adhesive thicknesses for a given adhesive modulus.

Figures 4-6 show that the interfacial shear stresses well satisfy the shear-free BCs at the right and left free-edges. Both the shear and peeling stresses exhibit stress concentrations near the free edges while quickly decaying to zero at a distance within around 20% the adhered thickness; such stress concentrations behave much more significant at the left edge than at the right edge. In addition, the free-edge interfacial shear stresses do not alter noticeably across the adhesive layer for all the cases under study; however, the free-edge interfacial peeling stresses vary abruptly across the adhesive layer up to 2 to 5 folds with the peak values all occurring at the upper interfaces. For the present ASSSJ, the upper steel cover layer is much stiffer (with less lateral deflections) than both the adhesive layer and Al-alloy adherents. Under the action of axial tensile forces applied to the lower Al-alloy adherents, a large bending moment exerts at the upper interface close to the left free-edge.

Correspondingly, a lower bending moment exerts at the right free-edge due to the lateral deflection of the slender Al-alloy adhered (with only 1/3 elastic modulus of steel). Therefore, the soft adhesive layer (with the elastic modulus only 1/14, 1/7, and 1/3.5 of Al-alloy) at the left free edge exerts large lateral deflections in order to maintain the static equilibrium of the slender structure, i.e., the high free-edge interfacial peeling stress at the upper interface. Thus, for all the cases, stress analysis as shown in Figures 4-6 predicts that debonding failure will initiate from the left free-edge of the upper adhesive-adhered interface, to be validated by CZM-based FEA in Subsection 2.2.

Moreover, Figures 4-6 also indicate the clear dependencies of the interfacial shear and peeling stresses upon the elastic modulus and thickness of the adhesive layer. When the adhesive thickness is fixed at either $h_0/h_2 = 0.1, 0.25, 0.35,$ and $0.5\,(h_2 = 2.0\text{mm})$, either the interfacial shear or the peeling stress increases slightly with increasing elastic modulus E_0 of the adhesive layer. This can be understood such that a softer adhesive layer (with a lower value of elastic modulus E_0) provides a relatively larger lateral deflection to suppress the bending moment due to loss of the lateral structural symmetry of the joint, i.e., the lower interfacial shear and peeling stresses. Furthermore, at fixed elastic modulus E_0 of the adhesive layer, in general, either the interfacial shear or peeling stress decreases by increasing thickness of the adhesive layer. In this case, a thicker adhesive layer corresponds to a larger lateral deformation of the adhesive layer due to the less lateral stiffness, which can consequently suppress the bending moment, i.e., the lower interfacial shear and peeling stresses, as predicted.

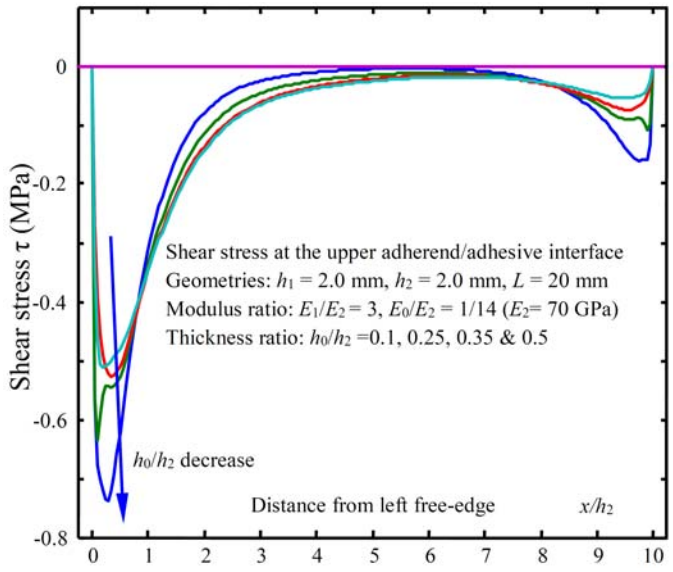
Shear stress τ (MPa)
0
-0.2
-0.4
-0.6
-0.8
Shear stress at the upper adherend/adhesive interface
Geometries: h_1 = 2.0 mm, h_2 = 2.0 mm, L = 20 mm
Modulus ratio: E_1/E_2 = 3, E_0/E_2 = 1/14 (E_2= 70 GPa)
Thickness ratio: h_0/h_2 =0.1, 0.25, 0.35 & 0.5
h_0/h_2 decrease
Distance from left free-edge
x/h_2
0 1 2 3 4 5 6 7 8 9 10

(a)

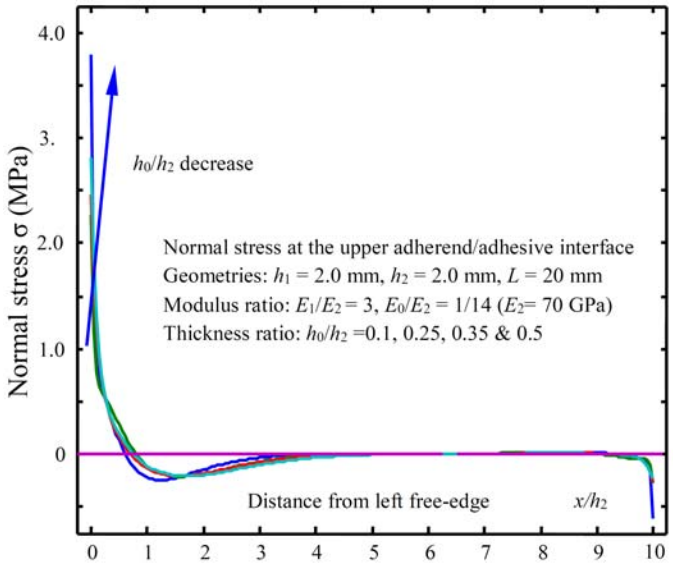
Normal stress σ (MPa)
4.0
3.
2.0
1.0
0
h_0/h_2 decrease
Normal stress at the upper adherend/adhesive interface
Geometries: h_1 = 2.0 mm, h_2 = 2.0 mm, L = 20 mm
Modulus ratio: E_1/E_2 = 3, E_0/E_2 = 1/14 (E_2= 70 GPa)
Thickness ratio: h_0/h_2 =0.1, 0.25, 0.35 & 0.5
Distance from left free-edge
x/h_2
0 1 2 3 4 5 6 7 8 9 10

(b)

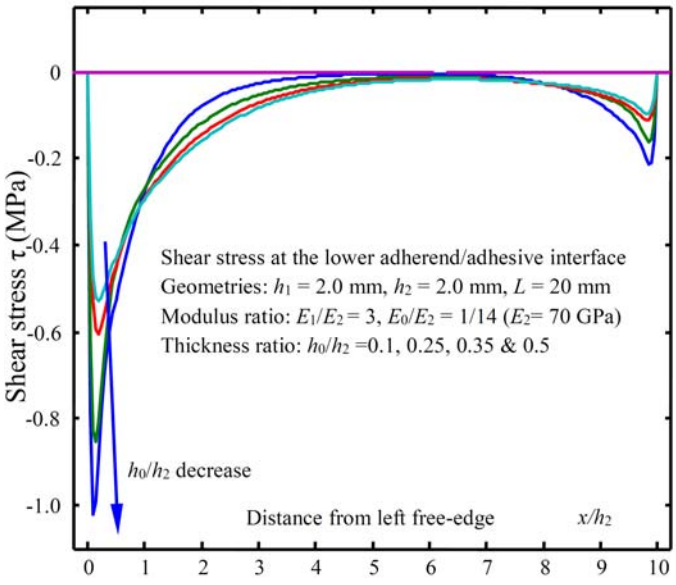

(c)

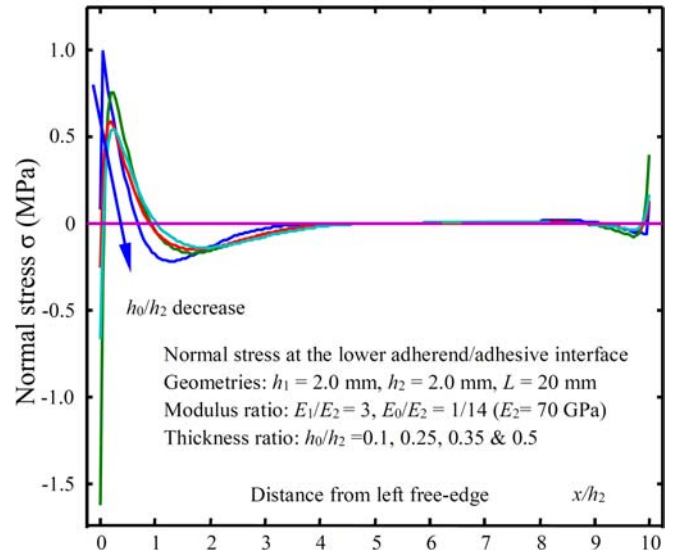

(d)

Figure 4. Variations of the interfacial shear and peeling stresses at the upper and lower interfaces between the adhered and adhesive layer of the ASSSJ at varying adhesive layer thickness. (Thickness ratio: $h_0 / h_2 = 0.1, 0.25, 0.35$ and 0.5; Modulus ratio: $E_1/E_2 = 3$, $E_0/E_2 = 1/14$, and $E_2 = 70$GPa.)

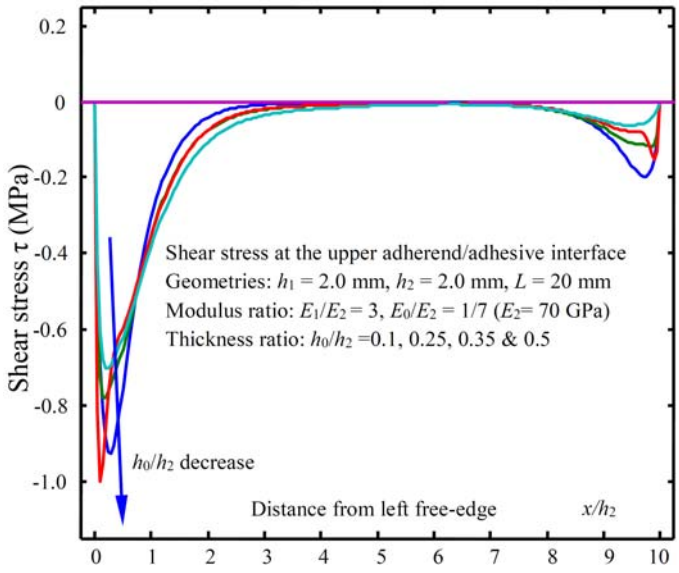
Shear stress τ (MPa)
0.2
0
-0.2
-0.4
-0.6
-0.8
-1.0
Shear stress at the upper adherend/adhesive interface
Geometries: h_1 = 2.0 mm, h_2 = 2.0 mm, L = 20 mm
Modulus ratio: E_1/E_2 = 3, E_0/E_2 = 1/7 (E_2= 70 GPa)
Thickness ratio: h_0/h_2 =0.1, 0.25, 0.35 & 0.5
h_0/h_2 decrease
Distance from left free-edge
x/h_2
0 1 2 3 4 5 6 7 8 9 10

(a)

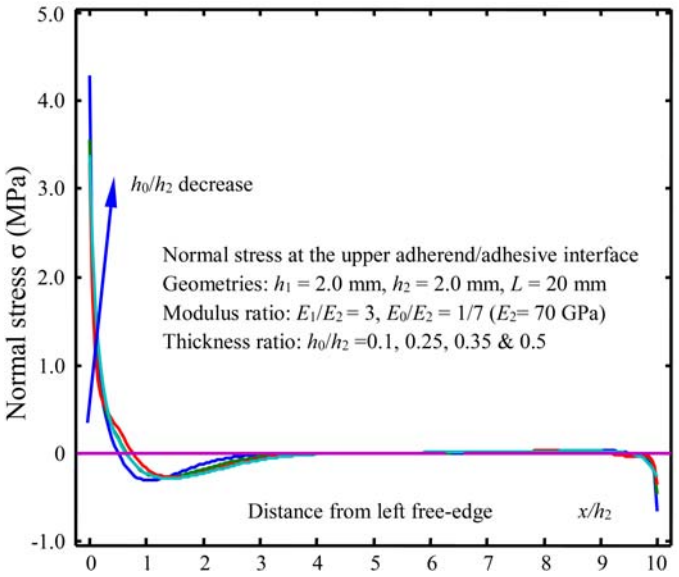
Normal stress σ (MPa)
5.0
4.0
3.0
2.0
1.0
0
-1.0
h_0/h_2 decrease
Normal stress at the upper adherend/adhesive interface
Geometries: h_1 = 2.0 mm, h_2 = 2.0 mm, L = 20 mm
Modulus ratio: E_1/E_2 = 3, E_0/E_2 = 1/7 (E_2= 70 GPa)
Thickness ratio: h_0/h_2 =0.1, 0.25, 0.35 & 0.5
Distance from left free-edge
x/h_2
0 1 2 3 4 5 6 7 8 9 10

(b)

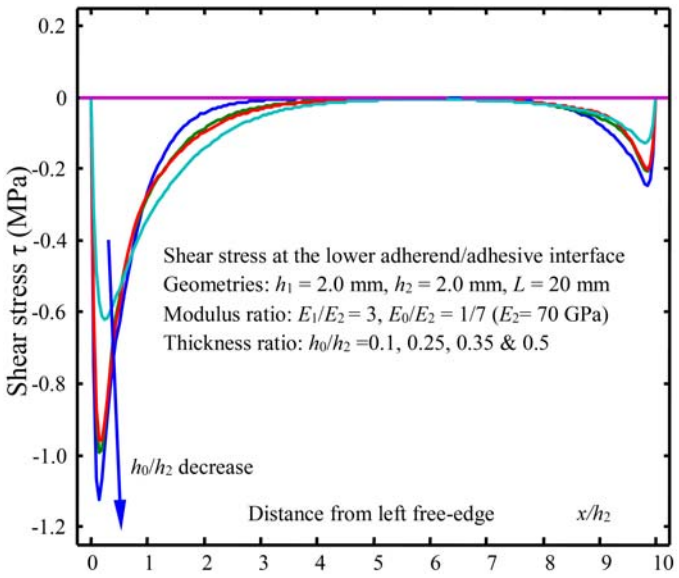

(c)

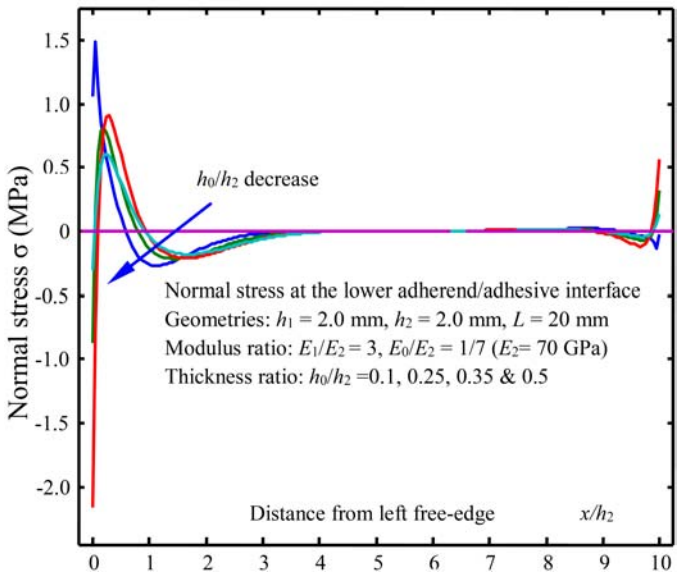

(d)

Figure 5. Variations of the interfacial shear and peeling stresses at the upper and lower interfaces between the adhered and adhesive layer of the ASSSJ at varying adhesive layer thickness. (Thickness ratio: h_0/h_2 = 0.1, 0.25, 0.35, and 0.5; Modulus ratio: E_1 / E_2 = 3, E_0 / E_2 = 1 / 7, and E_2 = 70GPa.)

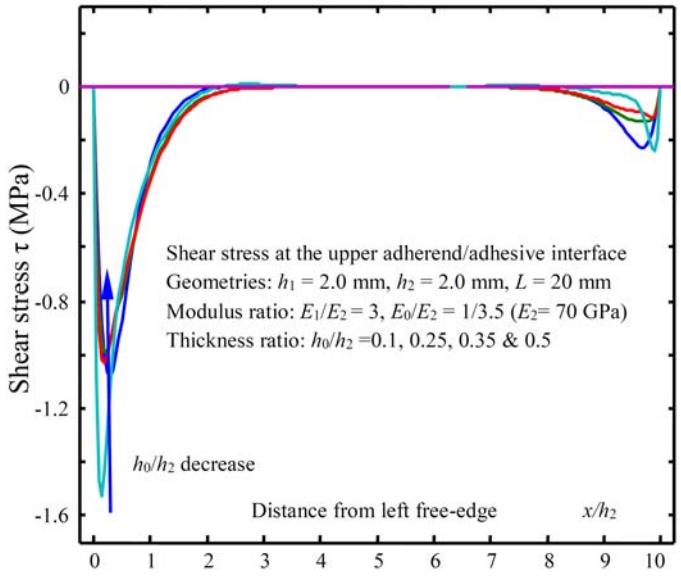
Shear stress τ (MPa)
0
-0.4
-0.8
-1.2
-1.6
Shear stress at the upper adherend/adhesive interface
Geometries: h_1 = 2.0 mm, h_2 = 2.0 mm, L = 20 mm
Modulus ratio: E_1/E_2 = 3, E_0/E_2 = 1/3.5 (E_2= 70 GPa)
Thickness ratio: h_0/h_2 =0.1, 0.25, 0.35 & 0.5
h_0/h_2 decrease
Distance from left free-edge
x/h_2
0 1 2 3 4 5 6 7 8 9 10

(a)

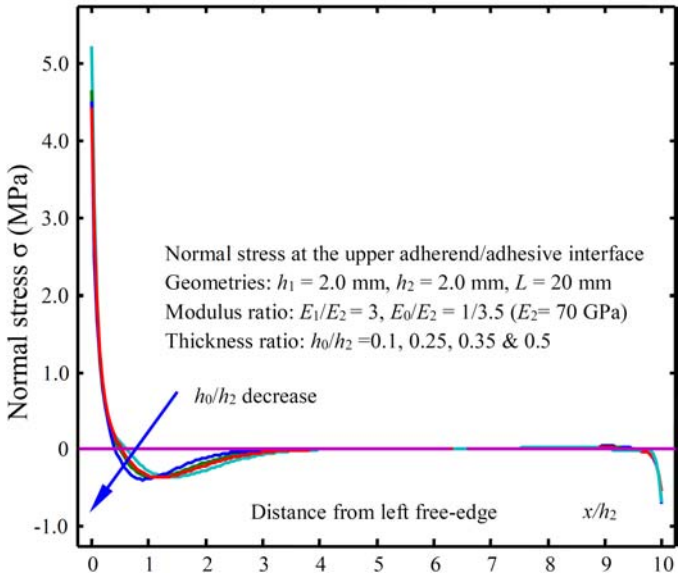
Normal stress σ (MPa)
5.0
4.0
3.0
2.0
1.0
0
-1.0
Normal stress at the upper adherend/adhesive interface
Geometries: h_1 = 2.0 mm, h_2 = 2.0 mm, L = 20 mm
Modulus ratio: E_1/E_2 = 3, E_0/E_2 = 1/3.5 (E_2= 70 GPa)
Thickness ratio: h_0/h_2 =0.1, 0.25, 0.35 & 0.5
h_0/h_2 decrease
Distance from left free-edge
x/h_2
0 1 2 3 4 5 6 7 8 9 10

(b)

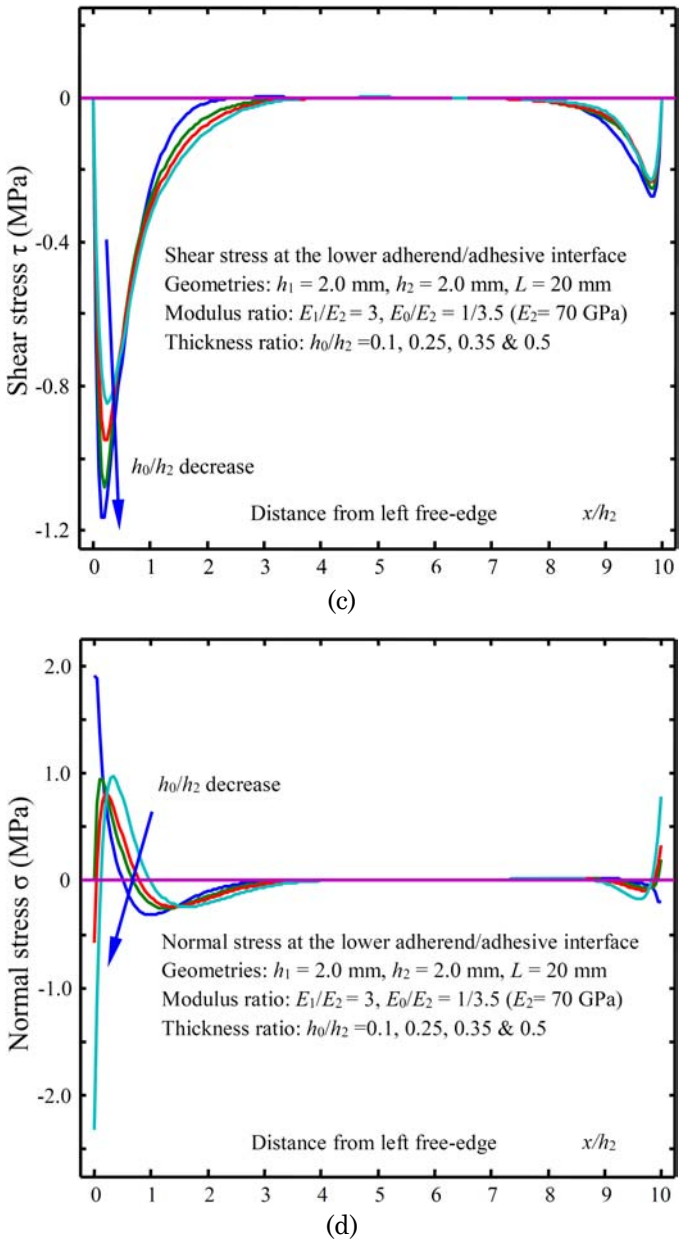

Figure 6. Variations of the interfacial shear and peeling stresses at the upper and lower interfaces between the adhered and adhesive layer of the ASSSJ at varying adhesive layer thickness. (Thickness ratio: $h_0/h_2 = 0.1, 0.25, 0.35,$ and 0.5; Modulus ratio: $E_1/E_2 = 3$, $E_0/E_2 = 1/3.5$, and $E_2 = 70$GPa.)

Besides, in principle, the stress field at the free-edge of bonded dissimilar materials behaves generally oscillating singular [5, 60-63] with the singularity exponent depending upon the material properties of bonded materials, i.e., *Dundurs' parameters* [64]. In the present approach, such oscillating singular behaviour of the stress field is not particularly approached as the interfacial stress functions were obtained naturally by solving a set of well-conditioned ODEs of the system via minimizing the complementary strain energy, which is similar to those semi-analytic approaches for determining the free-edge stresses in laminated composites [2, 3, 36, 37, 65-75]. In addition, various FEM approaches of the free-edge stress field in ABJs show that these free-edge interfacial shear and peeling stresses go up rapidly with refining meshes near the free edges, and such a varying tendency of the interfacial stresses is very close to the predictions by the stress-function variational methods [2, 3].

Furthermore, exploration of the oscillating singular stress field near free-edges of bonded materials is important to understand the nature of the stress field of ABJs. However, such oscillating singular stress field is inconvenient in practice to establish reliable and universal failure criteria to predict the debonding initiation and growth in ABJs. In addition, the stress-function variational method and other robust numerical methods are capable of accurately determining the stress filed near free edges of ABJs. But, these methods are not suitable for establishing the debonding criteria and modelling the debonding initiation and growth in ABJs. Alternatively, it is more convenient to utilize CZM-based FEA to directly simulate the debonding process of ABJs, in which the failure criterion is based on cohesive law. Thereafter, CZM-based FEA was employed to simulate the entire debonding process of the above ASSSJs subject to axial tensions and to extract the characteristic full-range force-displacement diagram and its dependency on the mechanical properties and geometries of the adhesive layer.

2.2. CZM-based modelling of interfacial debonding of ABJs

A number of CZMs have been successfully integrated into FEMs for high-efficiency, robust computational simulations of crack initiation, and growth in monolithic and composite materials. In the present study, the bilinear CZM available in ANSYS®(Version 16) [76] was utilized for modelling the entire debonding process in ASSSJs subjected to axial tension and exacting the corresponding full-range force-displacement diagram as the characteristic mechanical behaviour of ASSSJs useful for reliable design and failure prediction. As a matter of fact, debonding in ABJs is typically a mixed-mode fracture process, i.e., both the normal and tangential interfacial stresses at the bonding surfaces contribute to the total fracture energy of the ABJs. Thus, a power-law fracture criterion is typically used to define the completion of debonding as:

$$\left(\frac{G_I}{G_{IC}}\right)^2 + \left(\frac{G_{II}}{G_{IIC}}\right)^2 = 1, \tag{3}$$

where G_{IC} and G_{IIC} are the pure Mode-I and Mode-II fracture toughness, respectively, which are the interface properties of ABJs during a debonding event. G_I and G_{II} are, respectively, the pure Mode-I and Mode-II strain energy release rates, defined as the works done by the node normal and tangential forces during the complete node release process in CZM-based FEA of ABJ debonding:

$$G_I = \int_0^{\delta_n} \sigma_n d\delta_n, \tag{4}$$

and

$$G_{II} = \int_0^{\delta_t} \sigma_t d\delta_t. \tag{5}$$

In Equations (4) and (5), σ_n and δ_n are, respectively, the node normal stress and opening displacement, and σ_t and δ_t are, respectively, the node tangential stress and tangential opening displacement, as shown in

Figure 7(a). Variations of the node stresses σ_n and σ_t and the node displacements δ_n and δ_t were determined iteratively by the nonlinear numerical solving process of the FEM code, in which the $\sigma_n - \delta_n$ and $\sigma_t - \delta_t$ relations were assumed to follow the bilinear CZM as illustrated in Figure 7(b). In a bilinear CZM, the $\sigma_n - \delta_n$ and $\sigma_t - \delta_t$ diagrams consist of a linearly elastic loading region (*OA*) and a linearly elastic softening (*AC*). During the debonding process, the normal and shear nodal stresses reach the peak values at point *A*, and then softening happens and the normal and shear nodal forces linearly decrease to zero at *C*. The triangular area formed by *OAC* is the critical debonding toughness for either Mode-I or Mode-II. The control parameters of the bilinear CZM for either opening (Mode-I) or shear (Mode-II) failure are the normal (shear) force stiffness $k_n(k_t)$, peak normal (shear) stress (40MPa for the adhesive layer in this study), and critical Mode-I (II) debonding toughness $G_{IC}(G_{IIC})$.

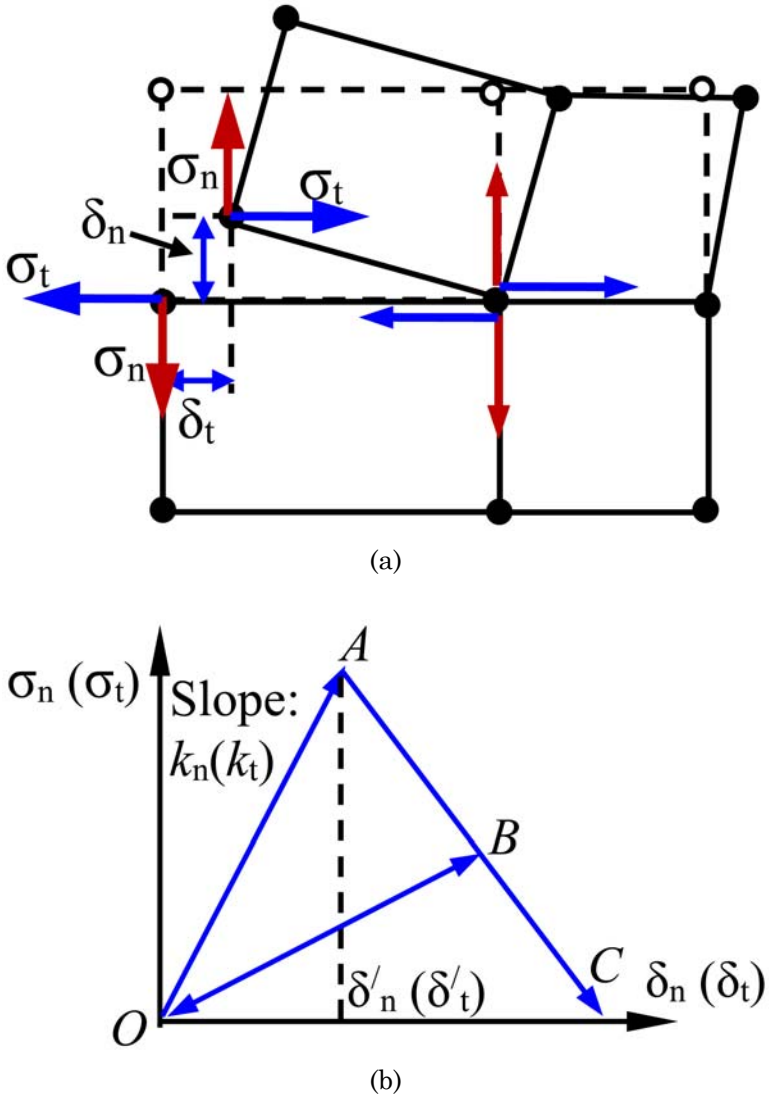

Figure 7. (a) Schematic node normal and tangential stresses and displacements in CZM-based FEM modelling of debonding process and (b) schematic $\sigma_n - \delta_n$ and $\sigma_t - \delta_t$ relations of a bilinear CZM.

In the present CZM-based FEA of the debonding process of an ASSSJ, the configuration of the ASSSJ was selected as the same as that used in Subsection 2.1 (as shown in Figure 2(b)), the left symmetric half-joint is considered in the numerical simulation. In this study, the main interest is to extract the full-range force-displacement diagram of the ASSSJ during the entire debonding process, especially the effects of the geometries and material properties of the adhesive layer including the thickness, Young's modulus, and interfacial debonding toughness (G_{IC} and G_{IIC}). Thus, for the CZM-based FEA, the geometries and material properties of the steel and Al-ally adherents of the ASSSJs were selected as the same as those in Subsection 2.1, while four thicknesses (h_0 = 0.2, 0.5, 07, and 1.0mm), four values of debonding toughness (G_{IC} = 0.25, 0.5, 0.75, and 1.0kJ/m^2 with G_{IIC} = 1.5 G_{IC}), and three Young's moduli (E_0 = 5, 10, and 15GPa) of the adhesive layers were selected for examining their influences on the mechanical behaviour of the ASSSJs during the debonding process. The failure stress of the adhesive layer was assumed as 40MPa. Herein, G_{IIC} of the adhesive layer was assumed to be 1.5 times G_{IC} of the adhesive layer for all the computational cases. This selection is based on the experimental observation of certain types of epoxy-based resin [36, 37]. In addition, ANSYS® (version 16) was used for the present computational study; four-node elements (PLANE182) and mapped uniform quadrilateral meshes were utilized for the entire ASSSJs, and two-node contact elements (CONTAC12) were introduced along both the upper and lower interfaces between the adherents and the adhesive layer. The minimum mesh size in the adhesive layer was controlled as one-tenth thickness of the adhesive layer, which shows very good numerical convergence and stability by comparison with results based on varying mesh sizes. The external tensile loads of the ASSSJs were exerted via fixing the horizontal displacements of the left end of the Al-alloy adhered as a constant value; the rest BCs of the ASSSJ follow the symmetric

conditions and removal of rigid-body motion. The rest options of the nonlinear numerical process were set as defaults by ANSYS®. As results, the debonding initiation and growth were determined by the CZM, meanwhile the effective axial tensile force of the ASSSJs were calculated by summing the horizontal nodal forces at the left end of the Al-alloy adhered. The latter forms the final full-range force-displacement diagram of the ASSSJ at varying geometries and material properties of the adhesive layer once the displacement of the left end of the Al-alloy adhered varies [77].

Figure 8 shows the typical configuration and Von Mises contour of the left symmetric half-joint in CZM-based FEA. It can be observed that debonding initiates and grows along the upper interface, corresponding to that predicted by the stress-function variational method in Subsection 2.1. Furthermore, Figures 9-11 give detailed numerical results of the full-range force-displacement diagrams and the onset and ultimate debonding forces of the ASSSJs at varying geometries and material properties of the adhesive layers. It can be noticed that under the action of axial tensile forces, the full-range force-displacement diagram of each ASSSJ during the entire debonding process consists of three regions, i.e., the beginning linearly elastic region prior to debonding initiation, the stable debonding growth region after the tensile force is higher than the debonding onset force, and the final unstable debonding region when the debonding growth reaches to the left end and catastrophic failure of the joint happens. The full-range force-displacement diagram of the ASSSJs during the debonding growth process is similar to that of typical ductile metals with a seemingly “yield” region and a “strain-hardening” region, which implies that ASSSJs carry excellent mechanical durability and toughness when treating debonding as “yielding”.

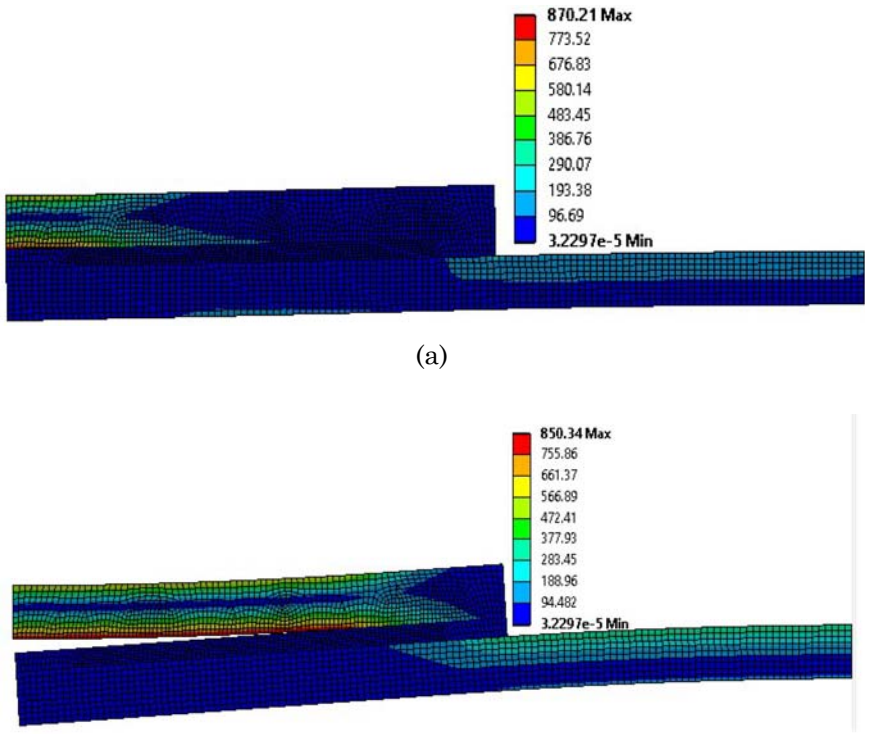

Figure 8. Typical configuration and Von Mises contour of the left symmetric half-joint in CZM-based FEA: (a) Prior to debonding and (b) after debonding growth.

Besides, Figures 9 and 10 show that at fixed Young's modulus of the adhesive layer (E_0 = 10GPa), the elastic stiffness of the ASSSJs prior to debonding slightly decreases with increasing thickness of the adhesive layer. This is because the elastic tangential compliance of the adhesive layer increases by increasing thickness of the adhesive layer. In addition, at fixed debonding toughness of the adhesive layer, the onset and ultimate debonding forces decrease by increasing thickness of the adhesive layer while the joint toughness (i.e., the area formed by the full-range force-displacement diagram) increases by increasing thickness of the adhesive layer. Such observations are resulted from the fact that the

thicker the adhesive layer, the more compliant the joint is, i.e., the larger joint deformation and larger toughness. Moreover, at fixed Young's modulus and thickness of the adhesive layer, the onset force for debonding initiation, ultimate tensile force, final axial displacement, and the toughness of the ASSSJ decrease significantly by decreasing debonding toughness of the adhesive layer. This observation indicates that the debonding toughness of the adhesive layer dominates the mechanical behaviour of the ASSSJs. Thus, superior debonding toughness of ABJs is highly desired and crucial to develop high-performance ABJs with high mechanical strength, durability, and toughness which can be achieved with various approaches from surface physics and chemistry to polymer science and engineering.

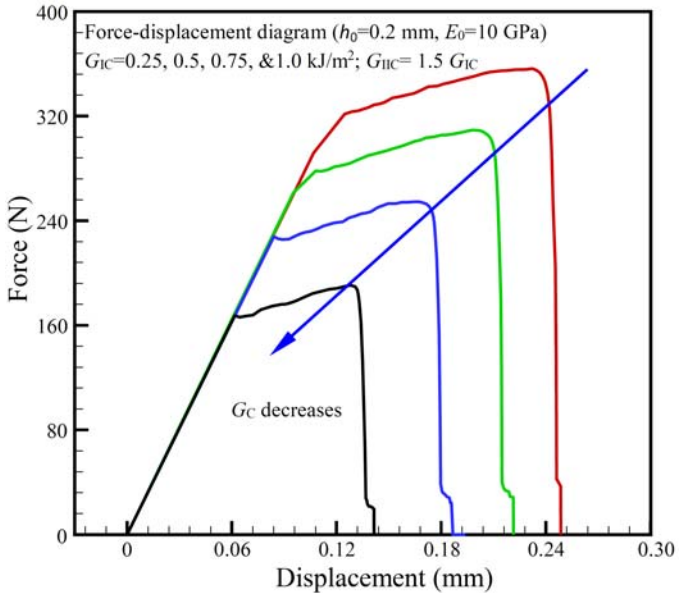
Force-displacement diagram (h_0=0.2 mm, E_0=10 GPa)
G_{IC}=0.25, 0.5, 0.75, &1.0 kJ/m^2; G_{IIC}= 1.5 G_{IC}
Force (N)
Displacement (mm)
G_C decreases
0
80
160
240
320
400
0.06
0.12
0.18
0.24
0.30

(a)

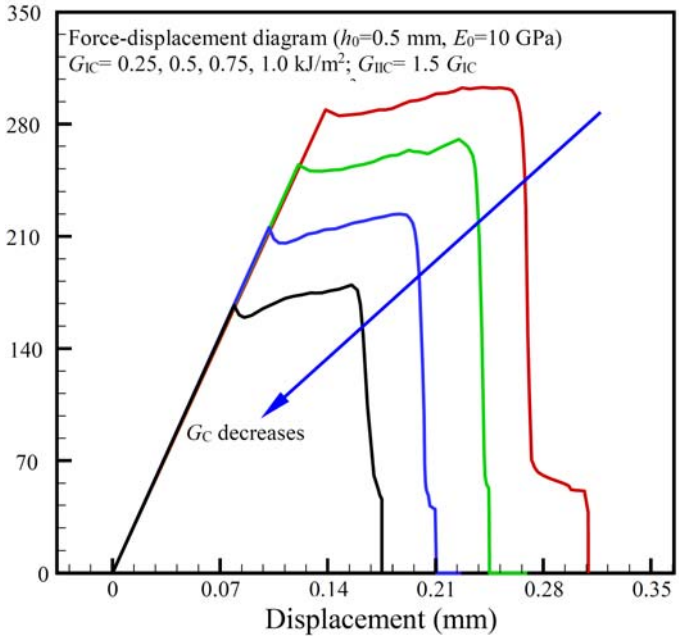
Force-displacement diagram (h_0=0.5 mm, E_0=10 GPa)
G_{IC}= 0.25, 0.5, 0.75, 1.0 kJ/m^2; G_{IIC}= 1.5 G_{IC}
Displacement (mm)
G_C decreases
0
70
140
210
280
350
0.07
0.14
0.21
0.28
0.35

(b)

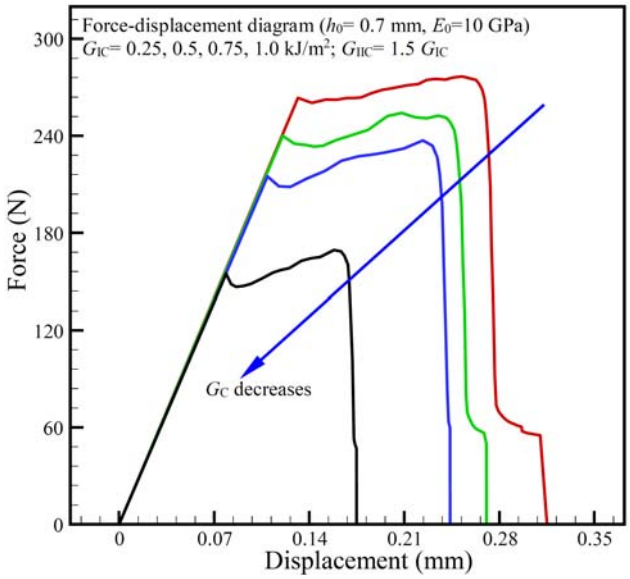

(c)

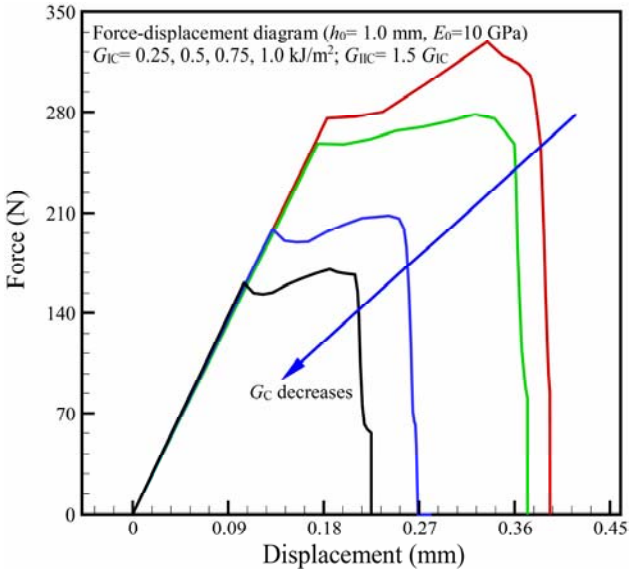

(d)

Figure 9. Predicted force-displacement diagrams of the ASSSJ at varying debonding toughness $[G_{IC} = 0.25(\text{black}), 0.5(\text{blue}), 0.75(\text{green}),$ and $1.0\text{kJ/m}^2(\text{red}), G_{IIC} = 1.5G_{IC}]$.

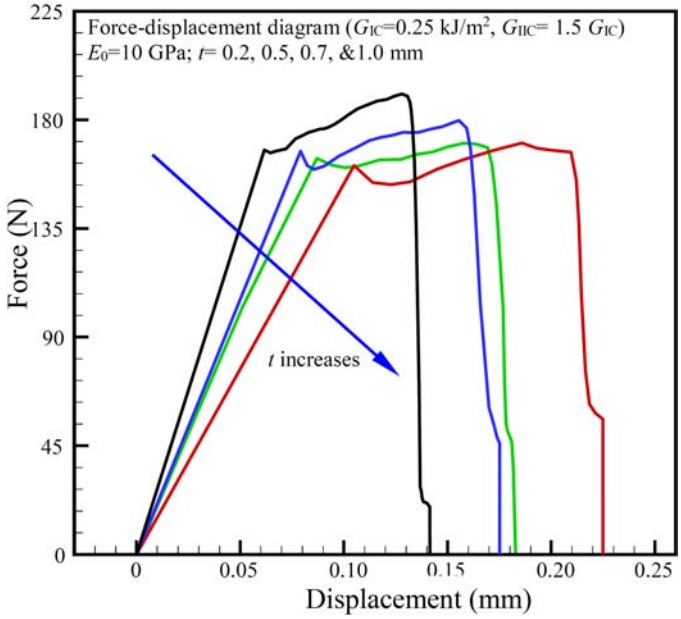
Force-displacement diagram (G_{IC}=0.25 kJ/m^2, G_{IIC}= 1.5 G_{IC})
E_0=10 GPa; t= 0.2, 0.5, 0.7, &1.0 mm
t increases
Force (N)
Displacement (mm)
0
45
90
135
180
225
0.05
0.10
0.15
0.20
0.25

(a)

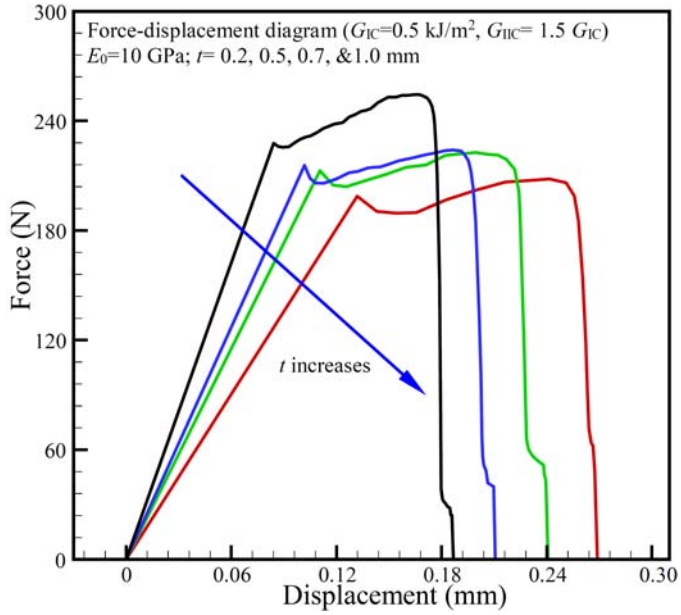
Force-displacement diagram (G_{IC}=0.5 kJ/m^2, G_{IIC}= 1.5 G_{IC})
E_0=10 GPa; t= 0.2, 0.5, 0.7, &1.0 mm
t increases
Force (N)
Displacement (mm)
0
60
120
180
240
300
0.06
0.12
0.18
0.24
0.30

(b)

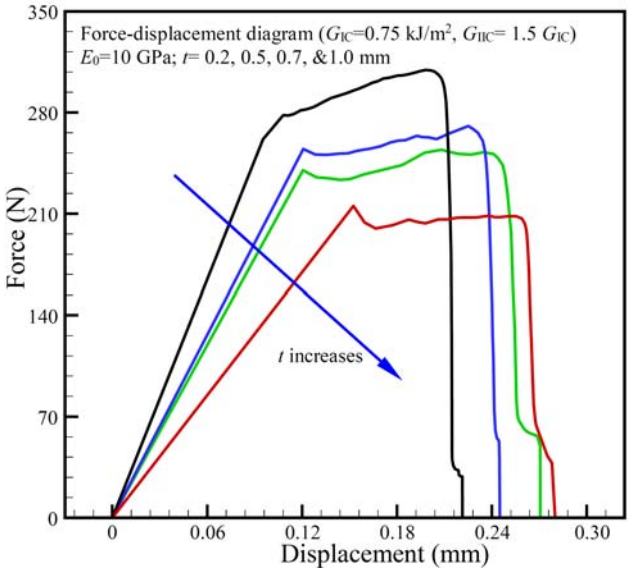

(c)

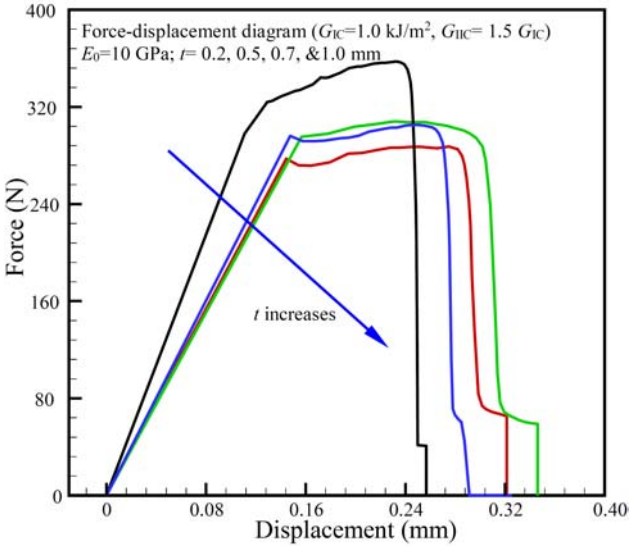

(d)

Figure 10. Predicted force-displacement diagrams of the ASSSJ at varying adhesive layer thickness [h_0 = 0.2 (black), 0.5 (blue), 0.7 (green), and 1.0mm(red)].

Additionally, Figure 11 shows that at fixed thickness and debonding toughness of the adhesive layer, the Young's modulus of the adhesive layer has no remarkable effect on the mechanical behaviour of the ASSSJs during the entire debonding growth process. This observation is resulted from the fact that comparatively, the Young's modulus of the adhesive layer is much lower than that of the steel and Al-alloy adherents, and therefore variation of the Young's modulus of the adhesive layer does not significantly alter the stress state of the ASSSJs in the present study. Consequently, Figure 12 summaries variations of the onset and ultimate debonding forces of the ASSSJs with respect to the debonding toughness of the ASSSJ at varying thickness (h_0 = 0.2, 0.5, and 0.7mm) and fixed Young's modulus (E_0 = 10GPa) of the adhesive layer, which are extracted from the diagrams shown in Figures 9 and 10. It can be found that the onset and ultimate debonding forces increases rapidly by increasing debonding toughness of the adhesive layer and decreases slightly by increasing thickness of the adhesive layer. These dependencies upon the thickness of the adhesive layer become more significant at the higher debonding toughness of the adhesive layer.

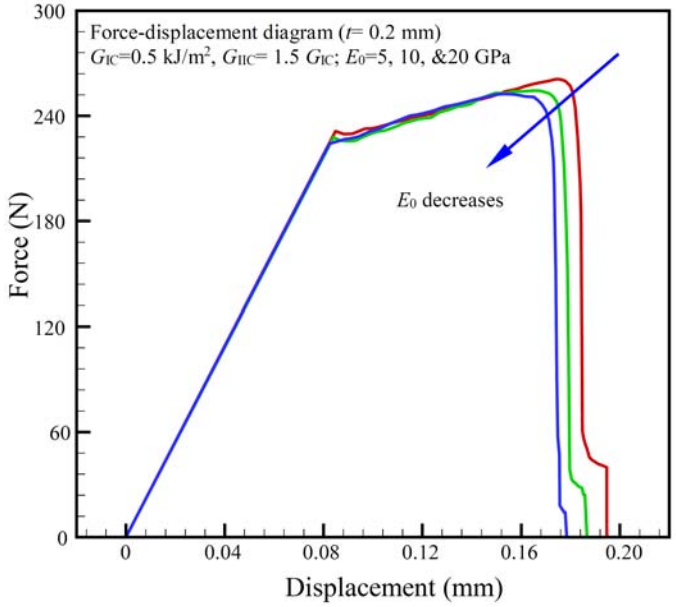
Force-displacement diagram (t= 0.2 mm)
G_{IC}=0.5 kJ/m^2, G_{IIC}= 1.5 G_{IC}; E_0=5, 10, &20 GPa
E_0 decreases
Force (N)
Displacement (mm)
0
60
120
180
240
300
0.04
0.08
0.12
0.16
0.20

(a)

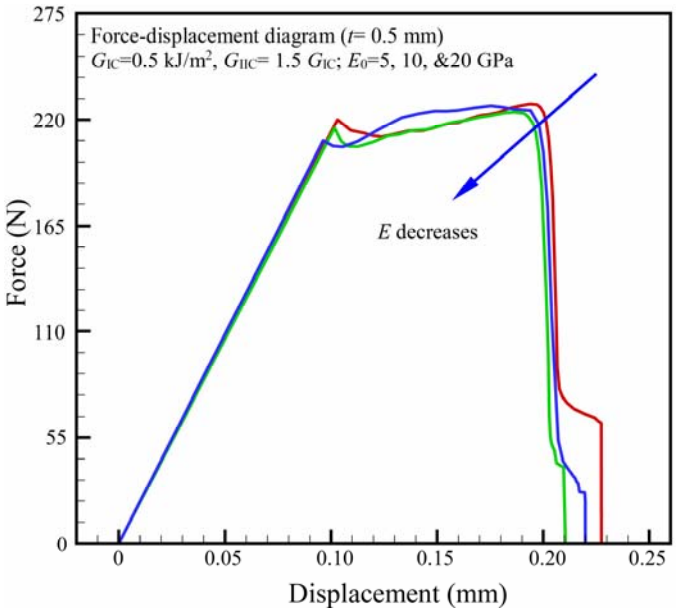
Force-displacement diagram (t= 0.5 mm)
G_{IC}=0.5 kJ/m^2, G_{IIC}= 1.5 G_{IC}; E_0=5, 10, &20 GPa
E decreases
Force (N)
Displacement (mm)
0
55
110
165
220
275
0.05
0.10
0.15
0.20
0.25

(b)

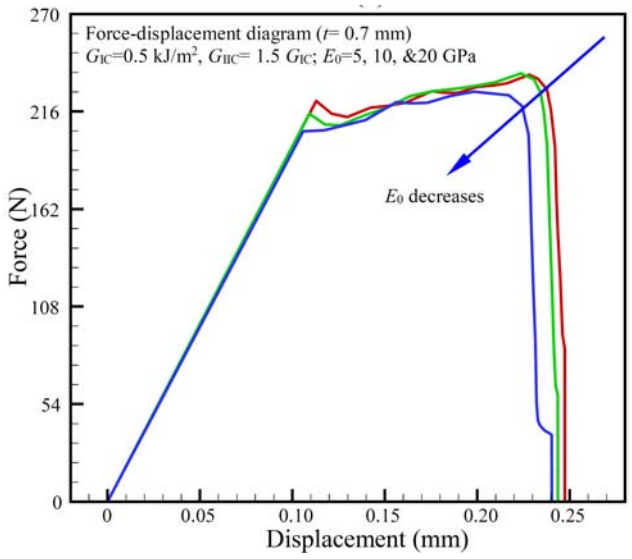

(c)

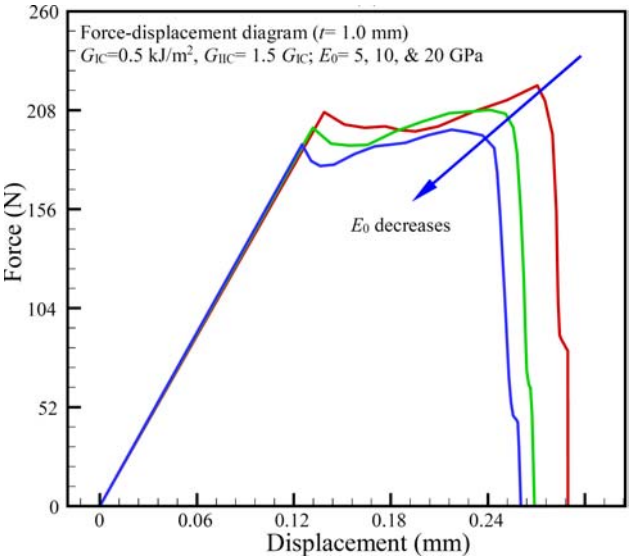

(d)

Figure 11. Predicted force-displacement diagrams of the ASSSJ at varying elastic modulus of the adhesive layer [E_0 = 2 (blue), 10 (green), and 20GPa (red)].

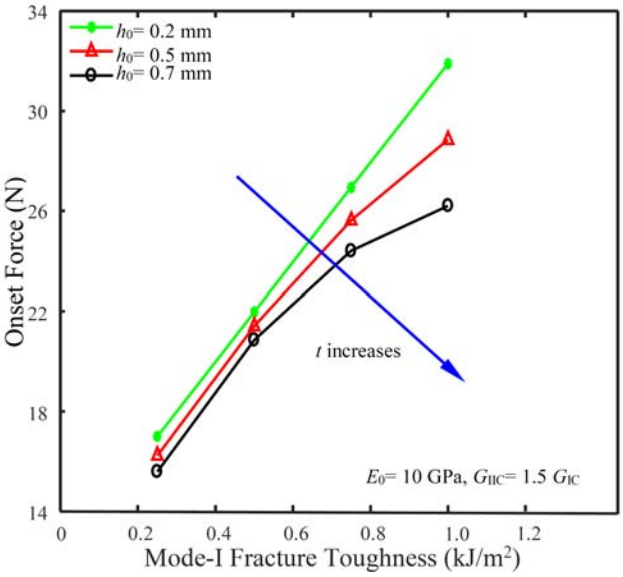

(a)

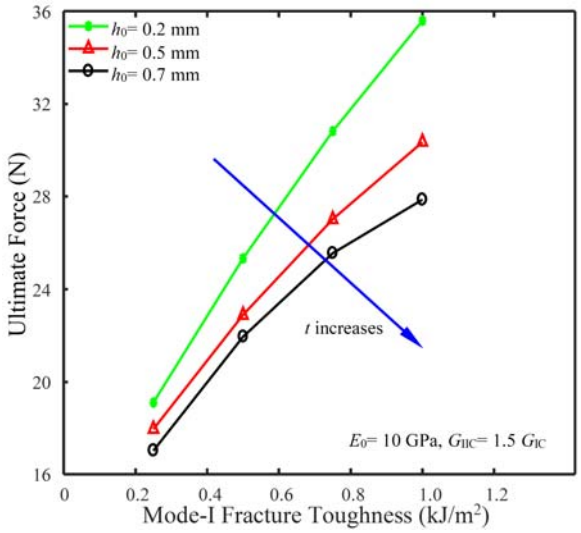

(b)

Figure 12. Variations of the debonding onset force: (a) and ultimate force and (b) with the debonding toughness of the ASSSJ at varying adhesive layer thickness [h_0 = 0.2 (green), 0.5 (red), and 0.7mm (black)].

The unique self-extension of the mechanical durability and toughness in ABJs can be utilized to avoid the catastrophic failure in adhesively bonded structures. Based on the robust stress-function variational method in Subsection 2.1, detailed stress analysis of ABJs indicated that the interfacial peeling and shear stresses in ABJs are highly localized at the free edges. Thus, a large portion of the bonded structure is functioned as redundant design to extend the service lifetime, durability, and toughness of bonded structures as demonstrated by the CZM-based FEA of the debonding process of ABJs in this study.

3. Concluding Remarks

The high-accuracy, robust semi-analytic stress-function variational method was successfully employed for interfacial stress analysis of a particular type of ABJs, i.e., the ASSSJs. Dependencies of the stress field of the ASSSJs upon the geometries and material properties of the adhesive layer were explored in detail. Debonding initiation happens at the free-edge with the highest interfacial peeling stress as predicted by the stress-function variation method and CZM-based FEA. Thus, these two different numerical methods employed in the present study can validate each other in some extent, which provide powerful tools for ABJ design and analysis.

The unique full-range force-displacement diagram of ABJs extracted from CZM-based FEA can be regarded as the characteristic diagram of ABJs, which behaves similar to that of ductile metals with three obviously identified regions, i.e., linearly elastic region, strain-hardening region, and unstable failure region. This characteristic force-displacement diagram can well explain the self-extension of the mechanical durability and toughness and can be used for reliable design and failure analysis and prediction of ABJs. The present computational study can be used as the theoretical basis of rational design, applications of ABJs, and broad adhesively bonded structures.

Acknowledgement

Partial support of the research by the ND NASA EPSCoR (NASA Grant # NNX07AK91A, seed grant: 43500-2490-FAR018640), Faculty Research Initiative Grant and the Department of Mechanical Engineering at NDSU is gratefully appreciated. X. Wu formulated the stress-function variational method for stress analysis of ABJs and wrote the manuscript; U. Chowdhury conducted the CZM-based FEA of ASSSJs.

References

[1] J. Tomblin and C. Davies, Bonded Structures Industry Survey, In: 2004 FAA Workshop on Bonded Structures, Seattle, WA, 2004.

[2] X. F. Wu and R. A Jenson, Stress-function variational method for stress analysis of bonded joints under mechanical and thermal loads, International Journal of Engineering Science 49(3) (2011), 279-294.

DOI: https://doi.org/10.1016/j.ijengsci.2010.11.005

[3] X. F. Wu and Y. Zhao, Stress-function variational method for interfacial stress analysis of adhesively bonded joints, International Journal of Solids and Structures 50(25-26) (2013), 4305-4319.

DOI: https://doi.org/10.1016/j.ijsolstr.2013.09.002

[4] X. F. Wu and U. Chowdhury, Fracture toughness of adhesively bonded joints with large plastic deformations, Engineering Fracture Mechanics 190 (2018), 16-30.

DOI: https://doi.org/10.1016/j.engfracmech.2017.11.040

[5] M. L. Williams, Stress singularities resulting from various boundary conditions in angular corners of plates in extension, Journal of Applied Mechanics: Transactions of ASME 19(4) (1952), 526-528.

[6] V. L. Hein and F. Erdogan, Stress singularities in a two-material wedge, International Journal of Fracture Mechanics 7(3) (1971), 317-330.

DOI: https://doi.org/10.1007/BF00184307

[7] P. S. Theocaris, The order of singularity at a multi-wedge corner of a composite plate, International Journal of Engineering Science 12(2) (1974), 107-120.

DOI: https://doi.org/10.1016/0020-7225(74)90011-1

[8] M. L. Dunn, W. Suwito and S. Cuningham, Stress intensities at notch singularities, Engineering Fracture Mechanics 57(4) (1997), 417-430.

DOI: https://doi.org/10.1016/S0013-7944(97)00019-2

[9] O. Volkersen, Die Nietkraftverleitung in zugbeanspruchten Nietverbindungen mit konstanten Laschenquerschnitten, Luftfahrtforschung 15 (1938), 41-47.

[10] M. Goland and E. Reissner, The stresses in cemented joints, Journal of Applied Mechanics: Transactions of ASME 11 (1944), 17-27.

[11] F. Delale, F. Erdogan and M. N. Aydinoglu, Stress in adhesively bonded joints: A closed-form solution, Journal of Composite Materials 15(3) (1981), 249-271.

DOI: https://doi.org/10.1177/002199838101500305

[12] Y. H. Zhao, Stress-Function Variational Method for Stress Analysis of Adhesively Bonded Joints (Thesis), North Dakota State University, North Dakota, USA, 2014.

[13] D. Chen and S. Cheng, An analysis of adhesive-bonded single-lap joints, Journal of Applied Mechanics 50(1) (1983), 109-115.

DOI: https://doi.org/10.1115/1.3166976

[14] F. Mortensen and O. T. Thomsen, Analysis of adhesive bonded joints: A unified approach, Composites Science and Technology 62(7-8) (2002), 1011-1131.

DOI: https://doi.org/10.1016/S0266-3538(02)00030-1

[15] J. Lee and H. Kim, Stress analysis of generally asymmetric single lap adhesively bonded joints, Journal of Adhesion 81(5) (2005), 443-472.

DOI: https://doi.org/10.1080/00218460590944918

[16] A. D. Diaz, R. Hadj-Ahmed, G. Foret and A. Ehrlacher, Stress analysis in a classical double lap, adhesively bonded joint with a layerwise model, International Journal of Adhesion and Adhesives 29(1) (2009), 67-76.

DOI: https://doi.org/10.1016/j.ijadhadh.2008.01.004

[17] S. C. Her, Stress analysis of adhesively-bonded lap joints, Composite Structures 47(1-4) (1999), 673-678.

DOI: https://doi.org/10.1016/S0263-8223(00)00052-0

[18] M. Y. Tsai, C. H. Hsu and C. N. Han, A note on Suhir's solution of thermal stresses for a die-substrate assembly, Journal of Electronic Packaging 126(1) (2004), 115-119.

DOI: https://doi.org/10.1115/1.1648056

[19] J. J. Radice and J. R. Vinson, On the analysis of adhesively bonded structures: A high order semi-elastic adhesive layer model, Composites Science and Technology 68(2) (2008), 376-386.

DOI: https://doi.org/10.1016/j.compscitech.2007.06.024

[20] M. A. Khan, S. Kumar and J. N. Reddy, Material-tailored adhesively bonded multilayers: A theoretical analysis, International Journal of Mechanical Sciences 148 (2018), 246-262.

DOI: https://doi.org/10.1016/j.ijmecsci.2018.08.017

[21] R. Hadj-Ahmed, G. Foret and A. Ehrlacher, Stress analysis in adhesive joints with a multiparticle model of multilayered materials (M4), International Journal of Adhesion and Adhesives 21(4) (2001), 297-307.

DOI: https://doi.org/10.1016/S0143-7496(00)00034-8

[22] S. A. Yousefsani and M. Tahani, Accurate determination of stress distributions in adhesively bonded homogeneous and heterogeneous double-lap joints, European Journal of Mechanics: A/Solids 39 (2013), 197-208.

DOI: https://doi.org/10.1016/j.euromechsol.2012.12.001

[23] S. A. Yousefsani and M. Tahani, Analytical solutions for adhesively bonded composite single-lap joints under mechanical loadings using full layerwise theory, International Journal of Adhesion and Adhesives 43 (2013), 32-41.

DOI: https://doi.org/10.1016/j.ijadhadh.2013.01.012

[24] S. A. Yousefsani and M. Tahani, Edge effects in adhesively bonded composite joint integrated with piezoelectric patches, Composite Structures 200 (2018), 187-194.

DOI: https://doi.org/10.1016/j.compstruct.2018.05.071

[25] Chang Fo-van, Thermal contact stresses of bi-metal strip thermostat, Applied Mathematics and Mechanics 4(3) (1983), 363-376.

DOI: https://doi.org/10.1007/BF01875669

[26] Chang Fo-van, Analysis of adhesive lap joint, Applied Mathematics and Mechanics 7(10) (1986), 937-945.

DOI: https://doi.org/10.1007/BF01907595

[27] Chang Fo-van, Interlaminar stresses of laminated composite joints with double cover plates, International Journal of Solids and Structures 26(2) (1990), 165-174.

DOI: https://doi.org/10.1016/0020-7683(90)90049-2

[28] Chang Fo-van, Interlaminar Stresses of Composite Materials (in Chinese), Beijing, China: High Education Press, 1993.

[29] F. Beer, E. R. Johnston, J. T. DeWolf and D. F. Mazurek, Mechanics of Materials (5th Edition), McGraw Hill, New York, USA, 2009.

[30] X. F. Wu and R. A. Jenson, Semianalytic stress-function variational approach for the interfacial stresses in bonded joints, Journal of Engineering Mechanics 140(11) (2014), 04014089.

DOI: https://doi.org/10.1061/(ASCE)EM.1943-7889.0000803

[31] R. A. Jenson, Stress-Function Varational Method and its Applications in the Strength Analysis of Bonded Joints and Hard Coatings (Thesis), North Dakota State University, North Dakota, USA, 2011.

[32] X. Wang, Stress-Function Varational Method for Stress Analysis of Adhesively Bonded Multilayer Composite Joints (Thesis), North Dakota State University, North Dakota, USA, 2015.

[33] S. Timoshenko and J. N. Goodier, Theory of Elasticity, McGraw-Hill, New York, NY, 1970.

[34] W. L. Yin, Free edge effects in anisotropic laminates under extension, bending and twisting, Part I: A stress-function-based variational approach, Journal of Applied Mechanics 61(2) (1994), 410-415.

DOI: https://doi.org/10.1115/1.2901459

[35] W. L. Yin, Free edge effects in anisotropic laminates under extension, bending and twisting, Part II: Eigenfunction analysis and the results for symmetric laminates, Journal of Applied Mechanics 61(2) (1994), 416-421.

DOI: https://doi.org/10.1115/1.2901460

[36] X. F. Wu, Fracture of Advanced Polymer Composites with Nanofiber Reinforced Interfaces (PhD Thesis), University of Nebraska-Lincoln, Lincoln, Nebraska, USA, 2003.

[37] X. F. Wu, Fracture of Advanced Composites with Nanostructured Interfaces: Fabrication, Characterization and Modeling, VDM Verlag, Germany, 2009.

[38] J. Custódio, J. Broughton and H. Cruz, A review of factors influencing the durability of structural bonded timber joints, International Journal of Adhesion and Adhesives 29(2) (2009), 173-185.

DOI: https://doi.org/10.1016/j.ijadhadh.2008.03.002

[39] L. F. M. da Silva, P. J. C. das Neves, R. D. Adams and J. K. Spelt, Analytical models of adhesively bonded joints, Part I: Literature survey, International Journal of Adhesion and Adhesives 29(3) (2009), 319-330.

DOI: https://doi.org/10.1016/j.ijadhadh.2008.06.005

[40] L. F. M. da Silva, P. J. C. das Neves, R. D. Adams, A. Wang and J. K. Spelt, Analytical models of adhesively bonded joints, Part II: Comparative study, International Journal of Adhesion and Adhesives 29(3) (2009), 331-341.

DOI: https://doi.org/10.1016/j.ijadhadh.2008.06.007

[41] S. Budhe, M. D. Banea, S. de Barros and L. F. M. da Silva, An updated review of adhesively bonded joints in composite materials, International Journal of Adhesion and Adhesives 72 (2017), 30-42.

DOI: https://doi.org/10.1016/j.ijadhadh.2016.10.010

[42] E. H. Wong and J. Liu, Interface and interconnection stresses in electronic assemblies: A critical review of analytical solutions, Microelectronics Reliability 79 (2017), 206-220.

DOI: https://doi.org/10.1016/j.microrel.2017.03.010

[43] Z. G. Suo and J. W. Hutchinson, Interface crack between two elastic layers, International Journal of Fracture 43(1) (1990), 1-18.

DOI: https://doi.org/10.1007/BF00018123

[44] J. W. Hutchinson and Z. Suo, Mixed mode cracking in layered materials, Advances in Applied Mechanics 29 (1991), 63-191.

DOI: https://doi.org/10.1016/S0065-2156(08)70164-9

[45] H. H. Yu, M. Y. He and J. W. Hutchinson, Edge effects in thin film delamination, Acta Materialia 49(1) (2001), 93-107.

DOI: https://doi.org/10.1016/S1359-6454(00)00293-7

[46] H. H. Yu and J. W. Hutchinson, Delamination of thin film strips, Thin Solid Films 423(1) (2003), 54-63.

DOI: https://doi.org/10.1016/S0040-6090(02)00973-2

[47] X. F. Wu and Y. A. Dzenis, Closed-form solution for the size of plastic zone in an edge-cracked strip, International of Journal of Engineering Science 40(15) (2002), 1751-1759.

DOI: https://doi.org/10.1016/S0020-7225(02)00031-9

[48] X. F. Wu and Y. A. Dzenis, Closed-form solution for a mode-III interfacial edge crack between two bonded dissimilar elastic strips, Mechanics Research Communications 29(5) (2002), 407-412.

DOI: https://doi.org/10.1016/S0093-6413(02)00317-8

[49] X. F. Wu, Y. A. Dzenis and T. Y. Fan, Two semi-infinite interfacial cracks between two bonded dissimilar elastic strips, International Journal of Engineering Science 41(15) (2003), 1699-1710.

DOI: https://doi.org/10.1016/S0020-7225(03)00107-1

[50] X. F. Wu, E. Lilla and W. S. Zou, A semi-infinite interfacial crack between two bonded dissimilar elastic strips, Archive of Applied Mechanics 72(8) (2002), 630-636.

DOI: https://doi.org/10.1007/s00419-002-0240-y

[51] X. F. Wu, Y. A. Dzenis and W. S. Zou, Interfacial edge crack between two bonded dissimilar orthotropic strips under antiplane point loading, Zeischrift für Angewandte Mathematik und Mechanik 83(6) (2003), 419-422.

DOI: https://doi.org/10.1002/zamm.200310063

[52] G. I. Barenblatt, The formation of equilibrium cracks during brittle fracture: General ideas and hypotheses, axially symmetric cracks, Journal of Applied Mathematics and Mechanics 23(3) (1959), 622-636.

DOI: https://doi.org/10.1016/0021-8928(59)90157-1

[53] G. I. Barenblatt, The mathematical theory of equilibrium cracks in brittle fracture, Advances in Applied Mechanics 7 (1962), 55-129.

DOI: https://doi.org/10.1016/S0065-2156(08)70121-2

[54] D. S. Dugdale, Yielding of steel sheets containing slits, Journal of the Mechanics and Physics of Solids 8(2) (1960), 100-104.

DOI: https://doi.org/10.1016/0022-5096(60)90013-2

[55] K. Park and G. H. Paulino, Cohesive zone models: A critical review of traction-separation relationships across fracture surfaces, Applied Mechanics Reviews 64(6) (2011), 1-20; Article 060802.

DOI: https://doi.org/10.1115/1.4023110

[56] P. Feraren and H. M. Jensen, Cohesive zone modelling of interface fracture near flaws in adhesive joints, Engineering Fracture Mechanics 71(15) (2004), 2125-2142.

DOI: https://doi.org/10.1016/j.engfracmech.2003.12.003

[57] P. A. Gustafson and A. M. Waas, The influence of adhesive constitutive parameters in cohesive zone finite element models of adhesively bonded joints, International Journal of Solids and Structures 46(10) (2009), 2201-2215.

DOI: https://doi.org/10.1016/j.ijsolstr.2008.11.016

[58] M. F. S. F. de Moura and J. P. M. Goncalves, Cohesive zone model for high-cycle fatigue of adhesively bonded joints under model I loading, International Journal of Solids and Structures 51(5) (2014), 1123-1131.

DOI: https://doi.org/10.1016/j.ijsolstr.2013.12.009

[59] M. A. S. Carneiro and R. D. S. G. Campilho, Analysis of adhesively-bonded *T*-joints by experimentation and cohesive zone models, Journal of Adhesion Science and Technology 31(18) (2017), 1998-2014.

DOI: https://doi.org/10.1080/01694243.2017.1291320

[60] T. C. T. Ting and S. C. Chou, Edge singularities in anisotropic composites, International Journal of Solids and Structures 17(11) (1981), 1057-1068.

DOI: https://doi.org/10.1016/0020-7683(81)90013-5

[61] S. S. Wang and I. Choi, Boundary-layer effects in composite laminates, Part 1: Free-edge stress singularities, Journal of Applied Mechanics 49(3) (1982), 541-548.

DOI: https://doi.org/10.1115/1.3162514

[62] S. S. Wang and I. Choi, Boundary-layer effects in composite laminates, Part 2: Free-edge stress solutions and basic characteristics, Journal of Applied Mechanics 49(3) (1982), 549-560.

DOI: https://doi.org/10.1115/1.3162521

[63] R. I. Zwiers, T. C. T. Ting and R. L. Spilker, On the logarithmic singularity of free-edge stress in laminated composites under uniform extension, Journal of Applied Mechanics 49(3) (1982), 561-469.

DOI: https://doi.org/10.1115/1.3162526

[64] J. Dundurs, Elastic Interaction of Dislocations with Inhomogeneities, In: Mathematics Theory of Dislocations (pp. 70-115), New York: American Society of Mechanical Engineering, 1968.

[65] R. B. Pipes and N. J. Pagano, Interlaminar stresses in composite laminates under uniform axial extension, Journal of Composite Materials 4(4) (1970), 538-548.

DOI: https://doi.org/10.1177/002199837000400409

[66] N. J. Pagano, On the calculation of interlaminar normal stress in composite laminate, Journal of Composite Materials 8(1) (1974), 65-81.

DOI: https://doi.org/10.1177/002199837400800106

[67] A. S. D. Wang and F. W. Crossman, Calculation of edge stresses in multi-layer laminates by sub-structuring, Journal of Composite Materials 12(1) (1978), 76-83.

DOI: https://doi.org/10.1177/002199837801200106

[68] C. Kassapoglou and P. A. Lagace, An efficient method for the calculation of interlaminar stresses in composite materials, Journal of Applied Mechanics 53(4) (1986), 744-750.

DOI: https://doi.org/10.1115/1.3171853

[69] L. Ye, Some characteristics of distributions of free-edge interlaminar stresses in composite laminates, International Journal of Solids and Structures 26(3) (1990), 331-351.

DOI: https://doi.org/10.1016/0020-7683(90)90044-V

[70] G. Flanagan, An efficient stress function approximation for the free-edge stresses in laminates, International Journal of Solids and Structures 31(7) (1994), 941-952.

DOI: https://doi.org/10.1016/0020-7683(94)90004-3

[71] C. Mittelstedt and W. Becker, Free-edge effects in composite laminates, Applied Mechanics Reviews 60(5) (2007), 217-245.

DOI: https://doi.org/10.1115/1.2777169

[72] X. F. Wu and Y. A. Dzenis, Experimental determination of probabilistic edge-delamination strength of a graphite-fiber/epoxy composite, Composite Structures 70(1) (2005), 100-108.

DOI: https://doi.org/10.1016/j.compstruct.2004.08.016

[73] X. F. Wu, Y. A. Dzenis and Emrah Gokdeg, Edge-cracked orthotropic bimaterial butt joint under antiplane singularity, International Journal of Nonlinear Science and Numerical Simulation 5(4) (2004), 347-354.

DOI: https://doi.org/10.1515/IJNSNS.2004.5.4.347

[74] X. F. Wu, R. A. Jenson and Y. Zhao, Stress-function variational approach to the interfacial stresses and progressive cracking in surface coatings, Mechanics of Materials 69(1) (2014), 195-203.

DOI: https://doi.org/10.1016/j.mechmat.2013.10.004

[75] B. Zhao, Z. H. Lu and Y. N. Lu, Closed-form solutions for elastic stress-strain analysis in unbalanced adhesive single-lap joints considering adherend deformations and bond thickness, International Journal of Adhesion and Adhesives 31(6) (2011), 434-445.

DOI: https://doi.org/10.1016/j.ijadhadh.2011.03.002

[76] ANSYS® Theory Reference (Version 16), Canonsburg, PA: ANSYS, Inc., 2016.

[77] U. Chowdhury, Theoretical and Computational Studies of the Strength and Fracture Toughness of Adhesively Bonded Joints and Polymer Nanoclay Composites (Thesis), North Dakota State University, North Dakota, USA, 2018.

■

Appendix

This Appendix is to summarize the stress-function variational method formulated by Wu and Zhao [3], which is further used for stress analysis of ASSSJs with varying stiffness and thickness of the adhesive layer in the present study. With the assumption that the axial stresses in the adherents and adhesive layer vary linearly across the thickness (i.e., *Euler-Bernoulli beams*), the rest shear and lateral normal stresses in the ASSSJs can be determined by evoking the stress equilibrium equations in 2D elasticity [33]. By minimizing the complementary strain energy of the ASSSJ segment, the four unknown interfacial stress functions f_1, f_2, g_1, and g_2 can be determined by solving a system of four coupled 4^{th}-order linear ODEs of constant coefficients [3]:

$$[A]\{\Phi^{(IV)}\} + [B]\{\Phi''\} + [C]\{\Phi\} + \{D\} = \{0\}. \tag{A1}$$

In the above, $\{\Phi\}_{4\times1}$ is a dimensionless interfacial stress function vector:

$$\{\Phi\} = \{F_1(\xi),\ G_1(\xi),\ F_2(\xi),\ G_2(\xi)\}^T, \tag{A2}$$

$$F_1(\xi) = F_1(x / h_2) = -\frac{1}{p_0 h_2}\int_0^x f_1(\zeta)d\zeta, \tag{A3}$$

$$F_2(\xi) = F_2(x / h_2) = -\frac{1}{p_0 h_2}\int_0^x f_2(\zeta)d\zeta, \tag{A4}$$

$$G_1(\xi) = G_1(x / h_2) = \frac{1}{p_0 h_2^2}\int_0^x\int_0^\zeta g_1(\eta)d\eta d\zeta, \tag{A5}$$

$$G_2(\xi) = G_2(x / h_2) = \frac{1}{p_0 h_2^2}\int_0^x\int_0^\zeta g_2(\eta)d\eta d\zeta. \tag{A6}$$

$[A]$, $[B]$, and $[C]$ are three 4×4 real-valued symmetric coefficient matrix that relate the elastic properties and layer thickness of the ASSSJ as

$[A]=$

$$\begin{bmatrix} \frac{1}{105}(h_{02}^3 e_{20} + h_{12}^3 e_{21}) & \frac{11}{210}(h_{02}^2 e_{20} - h_{12}^2 e_{21}) & -\frac{1}{140}h_{02}^3 e_{20} & \frac{13}{420}h_{02}^2 e_{20} \\ & \frac{13}{35}(h_{02} e_{20} + h_{12} e_{21}) & -\frac{13}{420}h_{02}^2 e_{20} & \frac{9}{70}h_{02} e_{20} \\ & & \frac{1}{105}(1 + h_{02}^3 e_{20}) & \frac{11}{210}(1 - h_{02}^2 e_{20}) \\ \text{Sys} & & & \frac{13}{35}(1 + h_{02} e_{20}) \end{bmatrix}, \tag{A7}$$

$[B]=$

$$\begin{bmatrix} -\frac{4}{15}(h_{02} e_{20} + h_{12} e_{21}) & \frac{1}{5}(-e_{20} + e_{21}) + \upsilon_0 e_{20} - \upsilon_1 e_{21} & \frac{1}{15}h_{02} e_{20} & \frac{1}{5}e_{20} \\ & -\frac{12}{5}(h_{02}^{-1} e_{20} + h_{12}^{-1} e_{21}) & -\frac{1}{5}e_{20} & \frac{12}{5}h_{02}^{-1} e_{20} \\ & & -\frac{4}{15}(1 + h_{02} e_{20}) & -\frac{1}{5}(1 - e_{20}) - \upsilon_0 e_{20} + \upsilon_2 \\ \text{Sys} & & & -\frac{12}{5}(1 + h_{02}^{-1} e_{20}) \end{bmatrix}, \tag{A8}$$

and

$[C]=$

$$\begin{bmatrix} 4(h_{02}^{-1} e_{20} + h_{12}^{-1} e_{21}) & 6(h_{02}^{-2} e_{20} - h_{12}^{-2} e_{21}) & 2h_{02}^{-1} e_{20} & -6h_{02}^{-2} e_{20} \\ & 12(h_{02}^{-3} e_{20} + h_{12}^{-3} e_{21}) & 6h_{02}^{-2} e_{20} & -12h_{02}^{-3} e_{20} \\ & & 4(1 + h_{02}^{-1} e_{20}) & 6(1 - h_{02}^{-2} e_{20}) \\ \text{Sys} & & & 12(1 + h_{02}^{-3} e_{20}) \end{bmatrix}, \tag{A9}$$

where

$$h_{02} = h_0 / h_2,\ h_{12} = h_1 / h_2,\ e_{20} = E_2 / E_0,\ e_{21} = E_2 / E_1. \tag{A10}$$

$\{D\}_{4\times1}$ is a dimensionless mechanical or thermomechanical load vector:

$$\{D\} = \{D_1,\ D_2,\ D_3,\ D_4\}^T, \tag{A11}$$

in which

$$D_1 = h_{12}^{-1}[1 + 3(1 + 2h_{02} + h_{12})h_{12}^{-2}]e_{21} + \frac{1}{2}(\alpha_1 - \alpha_0)\Delta T E_2 / p_0, \tag{A12}$$

$$D_2 = -\ 6(1 + 2h_{02} + h_{12})h_{12}^{-3}e_{21}, \tag{A13}$$

$$D_3 = -\frac{1}{2}(\alpha_2 - \alpha_0)\Delta T E_2 / p_0, \tag{A14}$$

$$D_4 = 0. \tag{A15}$$

Solution to (A1) can be obtained by superimposing the general solution $\{\Psi\}$ of the corresponding set of homogeneous ODEs onto a particular solution $\{\Phi_0\}$ [2]:

$$\{\Phi\} = \{\Psi\} + \{\Phi_0\}, \tag{A16}$$

$$[A]\{\Psi^{(IV)}\} + [B]\{\Psi^{//}\} + [C]\{\Psi\} = \{0\}, \tag{A17}$$

$$\{\Phi_0\} = -\ [C]^{-1}\{D\}. \tag{A18}$$

To solve the system of homogeneous ODEs (A17), consider the general solution $\{\Psi\}$ to carry the form:

$$\{\Psi\} = \{\Psi_0\}\exp(\lambda\xi), \tag{A19}$$

where λ and $\{\Psi_0\}$ are, respectively, the eigenvalue and eigenvector of the characteristic equation corresponding to (A17):

$$\lambda^4[A]\{\Psi_0\} + \lambda^2[B]\{\Psi_0\} + [C]\{\Psi_0\} = \{0\}. \tag{A20}$$

Equation (A20) is a generalized eigenvalue problem, which can be further converted into a standard eigenvalue problem by introducing:

$$\{\Psi_1\} = \lambda^2\{\Psi_0\}. \tag{A21}$$

Therefore, the generalized eigenvalue problem (A20) is reduced to a standard eigenvalue problem as follows:

$$\begin{bmatrix} I & 0 \\ 0 & A \end{bmatrix} \begin{Bmatrix} \Psi_0 \\ \Psi_1 \end{Bmatrix} = -\lambda^{-2} \begin{bmatrix} 0 & -I \\ C & B \end{bmatrix} \begin{Bmatrix} \Psi_0 \\ \Psi_1 \end{Bmatrix}, \tag{A22}$$

where I is a 4×4 identity. This standard eigenvalue problem can be routinely solved by means of popular numerical algorithms available in the literature [e.g., the eig( ) function available in Matlab™, etc.]. Finally, the formal solution (A16) can be expressed as:

$$\{\Phi\} = \sum_{k=1}^{8} [c_k \{\Psi_0^k\} \exp(\lambda_k \xi) + d_k \{\Psi_0^k\} \exp(-\lambda_k \xi)] + \{\Phi_0\}, \tag{A23}$$

where $\{\Psi_0^k\}$ $(k = 1, 2, \ldots, 8)$ are eigenvectors (the first 4 elements of each column) corresponding to eigenvalues $\lambda_k (k = 1, 2, \ldots, 8)$, respectively, and c_k and $d_k (k = 1, 2, \ldots, 8)$ are the 16 real-valued or complex coefficients to satisfy the 16 traction BCs at the adhered ends (A24)-(A39) [3]:

$$F_1(0) = 0, \tag{A24}$$

$$F_1(L / h_2) = -1, \tag{A25}$$

$$F_1'(0) = 0, \tag{A26}$$

$$F_1'(L / h_2) = 0, \tag{A27}$$

$$G_1(0) = 0, \tag{A28}$$

$$G_1(L / h_2) = 1 / 2 + h_{02}, \tag{A29}$$

$$G_1'(0) = 0, \tag{A30}$$

$$G_1'(L / h_2) = 0, \tag{A31}$$

$$F_2(0) = 0, \tag{A32}$$

$$F_2(L / h_2) = -1, \tag{A33}$$

$$F_2'(0) = 0, \tag{A34}$$

$$F_2'(L / h_2) = 0, \tag{A35}$$

$$G_2(0) = 0, \tag{A36}$$

$$G_2(L / h_2) = 1 / 2, \tag{A37}$$

$$G_2'(0) = 0, \tag{A38}$$

$$G_2'(L / h_2) = 0. \tag{A39}$$

Plugging (A23) into the 16 traction BCs (A24-A39) leads to a set of 16 simultaneous algebraic equations:

$$\sum_{k=1}^{8} c_k \Psi_0^{k,1} + \sum_{k=1}^{8} d_k \Psi_0^{k,1} = -\Phi_0^{(1)}, \tag{A40}$$

$$\sum_{k=1}^{8} c_k \Psi_0^{k,1} \exp(\lambda_k L / h_2) + \sum_{k=1}^{8} d_k \Psi_0^{k,1} \exp(-\lambda_k L / h_2) = -[1 + \Phi_0^{(1)}], \tag{A41}$$

$$\sum_{k=1}^{8} c_k \lambda_k \Psi_0^{k,1} - \sum_{k=1}^{8} d_k \lambda_k \Psi_0^{k,1} = 0, \tag{A42}$$

$$\sum_{k=1}^{8} c_k \lambda_k \Psi_0^{k,1} \exp(\lambda_k L / h_2) - \sum_{k=1}^{8} d_k \lambda_k \Psi_0^{k,1} \exp(-\lambda_k L / h_2) = 0, \tag{A43}$$

$$\sum_{k=1}^{8} c_k \Psi_0^{k,2} + \sum_{k=1}^{8} d_k \Psi_0^{k,2} = -\Phi_0^{(2)}, \tag{A44}$$

$$\sum_{k=1}^{8} c_k \Psi_0^{k,2} \exp(\lambda_k L / h_2) + \sum_{k=1}^{8} d_k \Psi_0^{k,2} \exp(-\lambda_k L / h_2) = 1/2 + h_{02} - \Phi_0^{(2)}, \tag{A45}$$

$$\sum_{k=1}^{8} c_k \lambda_k \Psi_0^{k,2} - \sum_{k=1}^{8} d_k \lambda_k \Psi_0^{k,2} = 0, \tag{A46}$$

$$\sum_{k=1}^{8} c_k \lambda_k \Psi_0^{k,2} \exp(\lambda_k L / h_2) - \sum_{k=1}^{8} d_k \lambda_k \Psi_0^{k,2} \exp(-\lambda_k L / h_2) = 0, \tag{A47}$$

$$\sum_{k=1}^{8} c_k \Psi_0^{k,3} + \sum_{k=1}^{8} d_k \Psi_0^{k,3} = -\Phi_0^{(3)}, \tag{A48}$$

$$\sum_{k=1}^{8} c_k \Psi_0^{k,3} \exp(\lambda_k L / h_2) + \sum_{k=1}^{8} d_k \Psi_0^{k,3} \exp(-\lambda_k L / h_2) = -[1 + \Phi_0^{(3)}], \tag{A49}$$

$$\sum_{k=1}^{8} c_k \lambda_k \Psi_0^{k,3} - \sum_{k=1}^{8} d_k \lambda_k \Psi_0^{k,3} = 0, \tag{A50}$$

$$\sum_{k=1}^{8} c_k \lambda_k \Psi_0^{k,3} \exp(\lambda_k L / h_2) - \sum_{k=1}^{8} d_k \lambda_k \Psi_0^{k,3} \exp(-\lambda_k L / h_2) = 0, \tag{A51}$$

$$\sum_{k=1}^{8} c_k \Psi_0^{k,4} + \sum_{k=1}^{8} d_k \Psi_0^{k,4} = -\Phi_0^{(4)}, \tag{A52}$$

$$\sum_{k=1}^{8} c_k \Psi_0^{k,4} \exp(\lambda_k L / h_2) + \sum_{k=1}^{8} d_k \Psi_0^{k,4} \exp(-\lambda_k L / h_2) = 1/2 - \Phi_0^{(4)}, \tag{A53}$$

$$\sum_{k=1}^{8} c_k \lambda_k \Psi_0^{k,4} - \sum_{k=1}^{8} d_k \lambda_k \Psi_0^{k,4} = 0, \tag{A54}$$

$$\sum_{k=1}^{8} c_k \lambda_k \Psi_0^{k,4} \exp(\lambda_k L / h_2) - \sum_{k=1}^{8} d_k \lambda_k \Psi_0^{k,4} \exp(-\lambda_k L / h_2) = 0. \tag{A55}$$

In the above, $\Psi_0^{k,1}$, $\Psi_0^{k,2}$, $\Psi_0^{k,3}$, and $\Psi_0^{k,4} (k = 1, 2, \ldots, 8)$ are, respectively, the 1st to 4th elements of the k-th eigenvector of the eigenvalue problem (A22); $\Phi_0^{(1)}$, $\Phi_0^{(2)}$, $\Phi_0^{(3)}$, and $\Phi_0^{(4)}$ are, respectively, the 1st to 4th elements of the particular solution vector $\{\Phi_0\}$. In particular, when the joint is subjected to a uniform temperature change ΔT and without mechanical loads, the right terms of traction BCs (A25), (A29), (A33), and (A37) are specified as zeros, which further influence the right terms of (A41), (A45), (A49), and (A53) accordingly. Once the 16 unknown coefficients $c_k (k = 1, 2, \ldots, 8)$ and $d_k (k = 1, 2, \ldots, 8)$ are determined by solving the above set of 16 linear algebraic equations (A40)-(A55) numerically, expressions (A2)-(A6), and (A23) finalize the four interfacial stress functions f_i (shear stress) and g_i (peeling stress) ($i = 1, 2$) as:

$$f_1(x) / p_0 = -\sum_{k=1}^{8} c_k \Psi_0^{k,1} \lambda_k \exp(\lambda_k x / h_2) + \sum_{k=1}^{8} d_k \Psi_0^{k,1} \lambda_k \exp(-\lambda_k x / h_2), \tag{A56}$$

$$g_1(x)/p_0 = \sum_{k=1}^{8} c_k \Psi_0^{k,2} \lambda_k^2 \exp(\lambda_k x / h_2) + \sum_{k=1}^{8} d_k \Psi_0^{k,2} \lambda_k^2 \exp(-\lambda_k x / h_2),$$

(A57)

$$f_2(x)/p_0 = -\sum_{k=1}^{8} c_k \Psi_0^{k,3} \lambda_k \exp(\lambda_k x / h_2) + \sum_{k=1}^{8} d_k \Psi_0^{k,3} \lambda_k \exp(-\lambda_k x / h_2),$$

(A58)

$$g_2(x)/p_0 = \sum_{k=1}^{8} c_k \Psi_0^{k,4} \lambda_k^2 \exp(\lambda_k x / h_2) + \sum_{k=1}^{8} d_k \Psi_0^{k,4} \lambda_k^2 \exp(-\lambda_k x / h_2).$$

(A59)